

# 1 On the use of GRACE normal equation of intersatellite tracking data for 2 improved estimation of soil moisture and groundwater in Australia

3 Natthachet Tangdamrongsub <sup>1</sup>, Shin-Chan Han <sup>1</sup>, Mark Decker <sup>2</sup>, In-Young Yeo <sup>1</sup>,  
4 Hyungjun Kim <sup>3</sup>

5 <sup>1</sup> School of Engineering, University of Newcastle, Callaghan, New South Wales, Australia

6 <sup>2</sup> ARC Centre of Excellence for Climate System Science, University of New South Wales,  
7 Sydney, New South Wales, Australia

8 <sup>3</sup> Institute of Industrial Science, the University of Tokyo, Tokyo, Japan  
9

## 10 Abstract

11 An accurate estimation of soil moisture and groundwater is essential for monitoring the  
12 availability of water supply in domestic and agricultural sectors. In order to improve the  
13 water storage estimates, previous studies assimilated terrestrial water storage variation  
14 ( $\Delta TWS$ ) derived from Gravity Recovery and Climate Experiment (GRACE) into land surface  
15 models. However, the GRACE-derived  $\Delta TWS$  was generally computed from the high level  
16 products (e.g., land grid from the Level 3 product). The gridded data products are subjected  
17 to several drawbacks such as signal attenuation and/or distortion caused by ad hoc posteriori  
18 filters, and a lack of error covariance information. The post-processing of GRACE data might  
19 lead to the undesired alteration of the signal and its statistical property. To exploit the  
20 GRACE information rigorously and negate these limitations, this study uses the fundamental  
21 GRACE satellite tracking Level 1B (L1B) data, not the post-processed  $\Delta TWS$  grid data. Our  
22 approach combines the GRACE's least-squares normal equation (full error variance-  
23 covariance information) of L1B data with the results from the Community Atmosphere Land  
24 Exchange (CABLE) model to improve soil moisture and groundwater estimates. This study  
25 demonstrates, for the first time, an importance of using the raw GRACE data. The GRACE-  
26 combine (GC) approach is developed for optimal least-squares combination maximizing the  
27 strength of the model and observations while suppressing the weaknesses. The approach is  
28 applied to estimate the soil moisture and groundwater over 10 Australian river basins and the  
29 results are validated against the satellite soil moisture observation and the in-situ groundwater  
30 data. We demonstrate the GC approach delivers evident improvement of water storage  
31 estimates, consistently from all basins, yielding better agreement at seasonal and inter-annual  
32 time scales. Significant improvement is found in groundwater storage while marginal  
33 improvement is observed in surface soil moisture estimates likely due to limitation of  
34 GRACE's temporal and spatial resolution.

## 36 1. Introduction

37 The changes of Terrestrial Water Storage ( $\Delta TWS$ ) derived from the Gravity Recovery And  
38 Climate Experiment (GRACE) data products have been used in the last decade to study  
39 global water resources, including groundwater depletion in India and Middle East (Rodell et  
40 al., 2009; Voss et al., 2013), water storage accumulation in Canada (Lambert et al., 2013),  
41 flood-influenced water storage fluctuation in Cambodia (Tangdamrongsub et al., 2016). The  
42 gravity data obtained from GRACE satellites are commonly processed and released in three

43 different product levels (L) that increase in the amount of processing, L1B – satellite tracking  
44 data (Wu et al., 2006), L2 – global gravitational Stokes coefficients (Bettadpur, 2012), and  
45 L3 – global grids (Landerer and Swenson, 2012). The original (L1B) GRACE information is  
46 inevitably altered or sheered due to data processing and successive post-processing filterings,  
47 because the error covariance information is not propagated through each post-processing step.

48 The GRACE-derived  $\Delta TWS$  has been computed widely from the higher-level products (e.g.,  
49 L2 and L3) on which various ad hoc post-processing filters were applied (e.g., Gaussian  
50 smoothing filter (Jekeli, 1981), destripe filter (Swenson and Wahr, 2006)).  $\Delta TWS$  obtained  
51 from these filters lacks proper error covariance information and is attenuated and distorted.  
52 To overcome the signal attenuation in GRACE high-level products, empirical approaches  
53 have been developed, including the application of scale factors computed from land surface  
54 models (Landerer and Swenson, 2012) to the GRACE L3 products. GRACE uncertainty in  
55 high level product is usually unknown or assumed. For example, Zaitchik et al. (2008)  
56 derived empirically a global average uncertainty that is variable depending on choices of  
57 post-processing filters (Sakumura et al., 2014). Furthermore, GRACE error and sensitivity is  
58 dependent on latitudes due to the orbit convergence toward poles (Wahr et al., 2006) and any  
59 post-processing filters will alter the GRACE data and their error information. Rigorous  
60 statistical error information is of equal importance to derivation of  $\Delta TWS$  for data  
61 assimilation and model calibration (Tangdamrongsub et al., 2017).  $\Delta TWS$  and its uncertainty  
62 estimates should be formulated directly from L1B data considering the complete statistical  
63 information.

64 The GRACE information is not fully exploited in many studies. For example, groundwater  
65 storage variation ( $\Delta GWS$ ) is often computed by subtracting the soil moisture variation ( $\Delta SM$ )  
66 component simulated by the land surface model from GRACE-derived  $\Delta TWS$  data (Rodell et  
67 al., 2009, Famiglietti et al., 2011), assuming the model  $\Delta SM$  is error-free. This may result in  
68 the inaccurate  $\Delta GWS$  and the associated error estimate as the uncertainties of GRACE and of  
69 the land surface model outputs are neglected in the combination of two noisy data. Several  
70 techniques have been developed to separate different signals considering the errors in  
71 GRACE and other data (Rietbroek et al., 2012; Schmeer et al., 2012; Forootan et al., 2017).  
72 However, the GRACE uncertainty is often derived empirically, not necessarily reflecting the  
73 actual GRACE error characteristics. The empirical GRACE errors have been also used in the  
74 data assimilation (e.g., Zaitchik et al., 2008; Tangdamrongsub et al., 2015; Tian et al., 2017).  
75 For example, Giroto et al. (2016) used L3 product and showed that it was necessary to adjust  
76 GRACE observation and its uncertainty in order to make their water storage estimates more  
77 accurate. Similarly, Tian et al. (2017) reported the need of applying a scale factor to GRACE  
78 uncertainty (from mascon product) in their GRACE assimilation process. It is apparent that  
79 the use of post-processed GRACE products often requires data tuning, leading possibly to an  
80 integration of incorrect gravity information into the data assimilation system. Some recent  
81 studies began to employ the full variance-covariance information in the data assimilation  
82 scheme (Eicker et al., 2014, Schumacher et al., 2016; Tangdamrongsub et al., 2017),  
83 however, the GRACE signal used were still affected by the post-processing filters.

84 This study aims to use the GRACE information of  $\Delta TWS$  measurement directly from the raw  
85 L1B data. The approach optimally combines the GRACE's least-squares normal equations  
86 with the model simulation results from the Community Atmosphere Land Exchange  
87 (CABLE, Decker, 2015) to improve  $\Delta SM$  and  $\Delta GWS$  estimates. The proposed approach

88 presents three main advantages. Firstly, one can exploit the full GRACE signal and error  
 89 information by using the normal equation data sets. Secondly, the approach is developed for  
 90 optimal least-squares combination, which maximizes the model and observation strength  
 91 while simultaneously suppressing their weaknesses. Finally, the method bypasses empirical,  
 92 multiple-step post-processing filters.

93 The main objective of this study is to present the GRACE-combined (GC) approach to  
 94 estimate improved  $\Delta SM$  and  $\Delta GWS$  at regional scales. We demonstrate our approach applied  
 95 to 10 Australian river basins (Fig. 1a). We validate the top layer of  $\Delta SM$  estimates against the  
 96 satellite soil moisture observation (the Advanced Microwave Scanning Radiometer aboard  
 97 EOS (AMSR-E), Njoku et al., 2003) over all 10 basins and the  $\Delta GWS$  estimates against the  
 98 in-situ groundwater data available over Queensland and Victoria (Fig. 1b, 1c).

99 This paper is outlined as follows: Firstly, the derivation of GC approach is presented in Sect.  
 100 2 while the description of GRACE data processing, including the use of GRACE normal  
 101 equation is given in Sect. 3. Secondly, the CABLE modelling is outlined in Sect. 4. This  
 102 includes the derivation of model uncertainty based on the quality of precipitation data and the  
 103 model parameter inputs. The processing of validation data is also described in Sect. 4.  
 104 Thirdly, Sect. 5 presents the result of  $\Delta SM$  and  $\Delta GWS$  estimates and comparison to in-situ  
 105 data. The long-term trends in the Australian mass variation over the last 13 years is also  
 106 investigated in this section.

107

## 108 **2. A method of combining GRACE L1B data with land surface model outputs**

109 The statistical information of  $\Delta TWS$  computed from a model can be written as:

$$110 \quad \tilde{\mathbf{h}} = \mathbf{h} + \boldsymbol{\epsilon}; \boldsymbol{\epsilon} \sim \mathcal{N}(\mathbf{0}, \mathbf{C}), \quad (1)$$

111 where  $\mathbf{h}$  is the “truth” (unknown) model state vector while  $\tilde{\mathbf{h}}$  is the calculated state vector  
 112 characterized with the model error  $\boldsymbol{\epsilon}$ . The model error is assumed to have zero mean and  
 113 covariance  $\mathbf{C}$ .

114 The term  $\mathbf{h}$  is used to represent a vector including global  $\Delta TWS$  grid, and terms with a  
 115 subscript  $R$  (e.g.,  $\mathbf{h}_R$ ,  $\mathbf{C}_R$ ) is used to represent only a regional set of  $\Delta TWS$  (for example, in  
 116 Australia). As such, the observation equation over a region can be rewritten as:

$$117 \quad \tilde{\mathbf{h}}_R = \mathbf{h}_R + \boldsymbol{\epsilon}; \boldsymbol{\epsilon} \sim \mathcal{N}(\mathbf{0}, \mathbf{C}_R). \quad (2)$$

118 As soil moisture and groundwater are the major components of  $\Delta TWS$  in Australia (surface  
 119 water storage being insignificant), the vector  $\mathbf{h}_R$  can be defined as:

$$120 \quad \mathbf{h}_R = [\Delta SM_{top} \quad \Delta SM_{rz} \quad \Delta GWS]^T, \quad (3)$$

121 where  $\Delta SM_{top}$ ,  $\Delta SM_{rz}$ ,  $\Delta GWS$  represent the vectors of top (surface) soil moisture, root zone  
 122 soil moisture, and groundwater storage variations, respectively.

123 A linearized GRACE satellite-tracking observation equation is formulated as:

$$124 \quad \mathbf{y} = \mathbf{A}\mathbf{x} + \mathbf{e}; \mathbf{e} \sim \mathcal{N}(\mathbf{0}, \boldsymbol{\Sigma}), \quad (4)$$

125 where  $\mathbf{y}$  is the observation vector containing various kinds of L1B data including the inter-  
 126 satellite ranging data,  $\mathbf{A}$  is the design (partial derivative) matrix relating the data and the  
 127 Earth gravity field variations,  $\mathbf{x}$  contains the Stokes coefficients of time-varying geopotential  
 128 fields (e.g., Wahr et al., 1998), and  $\mathbf{e}$  is the L1B data noise, which has zero mean and  
 129 covariance  $\mathbf{\Sigma}$ . Eq. (4) can be modified explicitly in terms of soil moisture and groundwater  
 130 storage variations as:

$$131 \quad \mathbf{y} = \mathbf{A}\mathbf{S}\bar{\mathbf{Y}}\mathbf{H}\mathbf{h} + \mathbf{e}; \mathbf{e} \sim \mathcal{N}(\mathbf{0}, \mathbf{\Sigma}), \quad (5)$$

132 where  $\mathbf{S}$  contains a factor used to convert  $\Delta TWS$  to geopotential coefficients considering the  
 133 load Love numbers (e.g., Wahr et al., 1998),  $\bar{\mathbf{Y}}$  converts the gridded data into the  
 134 corresponding spherical harmonic coefficients, and  $\mathbf{H}$  is the operational matrix converting  
 135  $\Delta\mathbf{SM}_{top}$ ,  $\Delta\mathbf{SM}_{rz}$ , and  $\Delta\mathbf{GWS}$  to  $\Delta TWS$ . This model is based on the assumption that the  
 136 GRACE orbital perturbation is a result of  $\Delta TWS$  variation on the surface, which is very  
 137 particular in Australia. For convenience, the term  $\mathbf{Y} = \mathbf{S}\bar{\mathbf{Y}}$  is used in the further derivation. If  
 138  $M$  is the number of model grid cells,  $N_{max}$  is the maximum degree of the geopotential  
 139 coefficients, and  $L=(N_{max}+1)^2-4$  is the number of geopotential coefficients, the dimension of  
 140  $\mathbf{Y}$ ,  $\mathbf{H}$ , and  $\mathbf{h}$  are  $L \times M$ ,  $M \times 3M$ , and  $3M \times 1$ , respectively.

141 A least-squares solution of Eq. (5) is given as:

$$142 \quad (\mathbf{H}^T\mathbf{Y}^T\mathbf{A}^T\mathbf{\Sigma}^{-1}\mathbf{A}\mathbf{Y}\mathbf{H})\hat{\mathbf{h}} = \mathbf{H}^T\mathbf{Y}^T\mathbf{A}^T\mathbf{\Sigma}^{-1}\mathbf{y}. \quad (6)$$

143 It can be simplified as:

$$144 \quad \mathbf{H}^T\mathbf{Y}^T\mathbf{N}\mathbf{Y}\mathbf{H}\hat{\mathbf{h}} = \mathbf{H}^T\mathbf{Y}^T\mathbf{c}, \quad (7)$$

145 where  $\mathbf{N} = \mathbf{A}^T\mathbf{\Sigma}^{-1}\mathbf{A}$  and  $\mathbf{c} = \mathbf{A}^T\mathbf{\Sigma}^{-1}\mathbf{y}$ . (The rationales of introducing  $\mathbf{N}$  and  $\mathbf{c}$  are explained  
 146 in the following section). Note that, the above derivations (Eq. (5) – Eq. (7)) are defined with  
 147 the global grid of  $\mathbf{h}$ . For a regional application, Eq. (7) can be modified as:

$$148 \quad \left[ \mathbf{H}_R^T\mathbf{Y}_R^T \mid \mathbf{H}_o^T\mathbf{Y}_o^T \right] \mathbf{N} \begin{bmatrix} \mathbf{Y}_R\mathbf{H}_R \\ \mathbf{Y}_o\mathbf{H}_o \end{bmatrix} \begin{bmatrix} \hat{\mathbf{h}}_R \\ \hat{\mathbf{h}}_o \end{bmatrix} = \left[ \mathbf{H}_R^T\mathbf{Y}_R^T \mid \mathbf{H}_o^T\mathbf{Y}_o^T \right] \mathbf{c}, \quad (8)$$

149 where the subscript  $R$  indicates the grid  $\Delta TWS$  only in a region of interest, and  $o$  for the rest  
 150 of the globe. If the number of the model grid cells associated with  $R$  is  $J$  and that of the  
 151 outside cells is  $M-J$ . As such, the dimensions of  $\mathbf{Y}_R$ ,  $\mathbf{H}_R$ ,  $\hat{\mathbf{h}}_R$ ,  $\mathbf{Y}_o$ ,  $\mathbf{H}_o$ ,  $\hat{\mathbf{h}}_o$  are  $L \times J$ ,  $J \times 3J$ ,  $3J \times 1$ ,  
 152  $L \times (M-J)$ ,  $(M-J) \times 3(M-J)$ ,  $3(M-J) \times 1$ , respectively. The dimension of  $\mathbf{N}$  and  $\mathbf{c}$  remain  
 153 unchanged, since they are essentially from the normal equations of the original GRACE L1B  
 154 data (to be discussed in the following section).

155 From Eq. (8), the normal equations associated with  $\Delta TWS$  in the region of interest can then  
 156 be written as

$$157 \quad \mathbf{H}_R^T\mathbf{Y}_R^T\mathbf{N}\mathbf{Y}_R\mathbf{H}_R\hat{\mathbf{h}}_R = \mathbf{H}_R^T\mathbf{Y}_R^T\mathbf{c} - \mathbf{H}_R^T\mathbf{Y}_R^T\mathbf{N}\mathbf{Y}_o\mathbf{H}_o\hat{\mathbf{h}}_o \quad (9)$$

158 or

$$159 \quad \mathbf{N}_R\hat{\mathbf{h}}_R = \mathbf{c}_R \quad (10)$$

160 where  $\mathbf{N}_R = \mathbf{H}_R^T\mathbf{Y}_R^T\mathbf{N}\mathbf{Y}_R\mathbf{H}_R$  and  $\mathbf{c}_R = \mathbf{H}_R^T\mathbf{Y}_R^T\mathbf{c} - \mathbf{H}_R^T\mathbf{Y}_R^T\mathbf{N}\mathbf{Y}_o\mathbf{H}_o\hat{\mathbf{h}}_o$ . As seen, Eq. (9) is the  
 161 regional representation of Eq. (7) where only the grid cells inside the study region are used,

162 while the contribution from the grid cells outside the region needs to be removed or  
 163 corrected. Combining the normal equation of Eq. (2) and Eq. (10), the optimal combined  
 164 solution of  $\hat{\mathbf{h}}_R$  can be resolved as follows:

$$165 \quad \hat{\mathbf{h}}_R = (\mathbf{C}_R^{-1} + \mathbf{N}_R)^{-1} (\mathbf{C}_R^{-1} \tilde{\mathbf{h}}_R + \mathbf{c}_R) \quad (11)$$

166 The computation of model covariance matrix  $\mathbf{C}_R$  will be discussed in Sect. 4.2. The posteriori  
 167 covariance of  $\hat{\mathbf{h}}_R$  can be estimated as follows:

$$168 \quad \hat{\Sigma} = (\mathbf{C}_R^{-1} + \mathbf{N}_R)^{-1}, \quad (12)$$

169 and the uncertainty estimate of  $\hat{\mathbf{h}}_R$  is simply calculated as:

$$170 \quad \sigma_{\hat{\mathbf{h}}} = \sqrt{\text{diag}(\hat{\Sigma})}, \quad (13)$$

171 where  $\text{diag}()$  represents the diagonal element of the given matrix.

172

### 173 3. GRACE data

#### 174 3.1 GRACE least-squares normal equations

175 In this study, the least-squares normal equations are obtained from the ITSG-Grace2016  
 176 products (Mayer-Gürr et al, 2016; <https://www.tugraz.at/institute/ifg/downloads/gravity-field-models/itsg-grace2016>) between January 2003 and March 2016. All L1B data including KBR  
 177 inter-satellite tracking data, attitude, accelerometer, GPS based kinematic orbit data and  
 178 AOD1B corrections are reduced in terms of the normal equations. These data products are  
 179 usually used to compute the Earth's geopotential field to the maximum harmonic degree and  
 180 order of 90, or at a spatial resolution of  $\sim 220$  km. The products contain the information of the  
 181 normal matrix  $\mathbf{N}$  and the vector  $\mathbf{c}$  (as shown in Eq. (7)) as well as the a-priori time-varying  
 182 gravity field coefficients predicted with the GOCO05s solution (Mayer-Gürr et al., 2015).  
 183 Note that the solution of the ITSG-Grace2016 normal equation is the anomalous geopotential  
 184 coefficient vector ( $\Delta\mathbf{x}$ ), which is referenced to the a-priori time-varying gravity field ( $\mathbf{x}_0$ ),  
 185 through:  
 186

$$187 \quad \mathbf{N} \Delta\mathbf{x} = \mathbf{d} \quad (14)$$

188 where  $\mathbf{d}$  and  $\mathbf{x}_0$  are given. To obtain a complete gravity field variation between the study  
 189 period ( $\mathbf{x}$  term in in Eq. (4)), the a-priori time-varying gravity field,  $\mathbf{x}_0$  is firstly restored to  
 190 Eq. (14), and the mean gravity field ( $\bar{\mathbf{x}}_0$ ) computed from all  $\mathbf{x}_0$  between January 2003 and  
 191 March 2016 is then removed as follows:

$$192 \quad \mathbf{N} (\Delta\mathbf{x} + \mathbf{x}_0 - \bar{\mathbf{x}}_0) = \mathbf{d} + \mathbf{N}(\mathbf{x}_0 - \bar{\mathbf{x}}_0) \quad (15)$$

$$193 \quad \mathbf{N} \mathbf{x} = \mathbf{d} + \mathbf{N}(\mathbf{x}_0 - \bar{\mathbf{x}}_0) \quad (16)$$

194 Therefore, in Sect. 2 (e.g., Eq. (7) – (11)), the matrix  $\mathbf{N}$  remains unchanged while the vector  $\mathbf{c}$   
 195 can be simply replaced by  $\mathbf{c} = \mathbf{d} + \mathbf{N}(\mathbf{x}_0 - \bar{\mathbf{x}}_0)$ .

196

#### 197 3.2 GRACE-derived $\Delta TWS$ products

198 Two monthly GRACE-derived  $\Delta TWS$  products are also used, the CNES/GRGS Release 3  
199 (RL3) (GRGS for short, Lemoine et al., 2015) and the JPL RL05M mascon-CRI version 2  
200 product (mascon for short, Watkins et al., 2015; Wiese et al., 2016). The GRGS solution  
201 provides  $\Delta TWS$  at  $1^\circ \times 1^\circ$  globally, derived from the Earth's geopotential coefficients up to the  
202 maximum degree and order 80, and no filter nor scale factor is applied (L2 data product).  
203 Mascon provides  $\Delta TWS$  at equal-area  $3^\circ$  spherical cap grid globally. In contrast to the GRGS  
204 solution, the mascon uses a gain factor derived from the land surface model (LSM) to restore  
205 mitigated signals and reduce leakage errors (L3 data products) (Watkins et al., 2015; Wiese et  
206 al., 2016). Additionally, mascon provides the  $\Delta TWS$  uncertainty together with the solution.  
207 The uncertainty is computed based on several geophysical models (see Watkins et al. (2015)  
208 and Wiese et al. (2016) for more details). The uncertainty information is not available in the  
209 GRGS product.

210 The  $\Delta TWS$  products are obtained between January 2003 and March 2016. The GRGS  
211 solution is retrieved from [http://grgs.obs-mip.fr/grace/variable-models-grace-lageos/grace-](http://grgs.obs-mip.fr/grace/variable-models-grace-lageos/grace-solutions-release-03)  
212 [solutions-release-03](http://grgs.obs-mip.fr/grace/variable-models-grace-lageos/grace-solutions-release-03) while the mascon is from [http://grace.jpl.nasa.gov/data/get-](http://grace.jpl.nasa.gov/data/get-data/jpl_global_mascons)  
213 [data/jpl\\_global\\_mascons](http://grace.jpl.nasa.gov/data/get-data/jpl_global_mascons). After retrieval, the long-term mean value between January 2003  
214 and March 2016 is computed and subtracted from the monthly products. To be consistent  
215 with CABLE grid spacing (see Sect. 4), the spatial resolution of two datasets are resampled to  
216  $0.5^\circ \times 0.5^\circ$  using the nearest grid values.

217 In this study, these two independent GRACE solutions are used for two main reasons:

- 218 1. To obtain the  $\Delta TWS$  values outside Australia. As shown in Eq. (9), the  $\hat{h}_o$  vector  
219 needs to be known, which can be from the GRACE-derived  $\Delta TWS$  solution. We use  
220 the GRGS solutions as the GRGS solution provides  $\Delta TWS$  at a spatial resolution  
221 comparable to the normal equation data.
- 222 2. To compare with the  $\Delta TWS$  estimates from our approaches. Both GRGS and JPL  
223 mascon solutions are used to compare and validate our  $\Delta TWS$  estimates.

224  
225

## 226 **4. Hydrology model and validation data**

### 227 **4.1 Model setup**

228 The extensive description of the CABLE model is given in Decker (2015) and Ukkola et al.  
229 (2016). This section describes the model setup and specific changes applied for this study.  
230 CABLE can be used to estimate soil moisture and groundwater in terms of volumetric water  
231 content every 3 hours at a  $0.5^\circ \times 0.5^\circ$  spatial resolution. The soil moisture and groundwater  
232 storage can be simply computed by multiplying the estimates with thicknesses of various  
233 layers. For soil moisture, the thickness of 6 soil layers is 0.022, 0.058, 0.154, 0.409, 1.085,  
234 and 2.872 m, from top to bottom, respectively. The thickness of the groundwater layer is  
235 modelled to be 20 m uniformly. Recalling Eq. (3),  $\Delta SM_{top}$  is defined as the soil moisture  
236 storage variation at the top 0.022 m thick layer, while  $\Delta SM_{rz}$  is the variation accumulated  
237 over the second to the bottom soil layers (depth between 0.022 m and 4.6 m).

238 CABLE is initially forced with the data from the Global Soil Wetness Project Phase 3  
239 (GSWP3), which is currently available until December 2010 (<http://hydro.iis.u->

240 [tokyo.ac.jp/GSWP3](http://tokyo.ac.jp/GSWP3), <https://doi.org/10.20783/dias.501>). We replace GSWP3 forcing data  
 241 with GLDAS data (Rodell et al., 2004) to compute the water storage changes to 2016. The  
 242 forcing data used in CABLE are precipitation, air temperature, snowfall rate, wind speed,  
 243 humidity, surface pressure, and short-wave and long-wave downward radiations. To  
 244 investigate the impact of different forcing data, the offline sensitivity study is conducted by  
 245 comparing the water storage estimates computed using:

- 246 1. All 8 forcing data components of GSWP3,
- 247 2. GSWP3 data with replacing one component obtained from GLDAS forcing data.

248 It is found that the water storage estimate is most sensitive to the replacement of precipitation  
 249 data, as expected, and relatively less sensitive to the change of other forcing components. We  
 250 use the GLDAS forcing data in this study and also further test 7 different precipitation data  
 251 products (see more details in Sect. 4.2). The forcing data are up/down sampled to a  $0.5^\circ \times 0.5^\circ$   
 252 spatial grid to reconcile with the CABLE spatial resolution.  
 253

## 254 4.2 Model uncertainty

255 In this study, the CABLE uncertainty is derived from 210 ensemble estimates associated with  
 256 different forcing data and model parameters. The 7 different precipitation products (see Table  
 257 1) are used to run the model independently. Most products are available to present day while  
 258 GSWP3, Princeton, and MERRA are only available until December 2010, December 2012,  
 259 and February 2016, respectively. For each precipitation forcing, 30 ensembles are generated  
 260 by perturbing the model parameters within  $\pm 10\%$  of the nominal values. The perturbed size  
 261 of 10% is similar to Dumedah and Walker (2014). Based on the CABLE structure, the  $\Delta SM$   
 262 and  $\Delta GWS$  estimates are most sensitive to the model parameters listed in Table 2. For  
 263 example, the fractions of clay, sand, and silt ( $f_{clay}$ ,  $f_{sand}$ ,  $f_{silt}$ ) are used to compute soil  
 264 parameters including field capacity, hydraulic conductivity, and soil saturation which mainly  
 265 affect soil moisture storage. Similarly, the drainage parameters (e.g.,  $q_{sub}$ ,  $f_p$ ) control the  
 266 amount of subsurface runoff, which has a direct impact on root zone soil moisture and  
 267 groundwater storages.

268 From ensemble generations, total  $K = 210$  sets of the ensemble water storage estimates ( $\mathbf{h}_e$ )  
 269 are obtained:

$$270 \quad \mathcal{H}_R = [\mathbf{h}_e|_{k=1} \quad \mathbf{h}_e|_{k=2} \quad \mathbf{h}_e|_{k=3} \quad \dots \quad \mathbf{h}_e|_{k=K}] \quad (17)$$

271 and the mean value of  $\mathcal{H}_R$  is computed as follows:

$$272 \quad \tilde{\mathbf{h}}_R = \frac{1}{K} \sum_{k=1}^K \mathbf{h}_e|_k \quad (18)$$

273 Note that due to the absence of GSWP3, Princeton, and MERRA data, the number of  
 274 ensembles reduce to  $K = 180$  after December 2010,  $K = 150$  after December 2012, and  $K =$   
 275  $120$  after February 2016, respectively. The GC approach assumes that model errors are  
 276 normally distributed with zero mean. Any violation of this assumption will yield a bias in the  
 277 combined solutions. Therefore, the mean value is removed from each ensemble member,

278  $\mathcal{H}_R' = \mathcal{H}_R - \tilde{\mathbf{h}}_R$ , and the error covariance matrix of the model is empirically computed as:

$$279 \quad \mathbf{C}_R = \mathcal{H}_R' (\mathcal{H}_R')^T / (K - 1) \quad (19)$$

280 The  $\tilde{\mathbf{h}}_R$  (Eq. (18)) and  $\mathbf{C}_R$  (Eq. (19)) terms can be directly used in Eq. (11).

281 Note that the sampling error caused by finite sample size might lead to spurious correlations  
282 in the model covariance matrix (Hamill et al., 2001). The effect can be reduced by applying  
283 an exponential decay with a particular spatial correlation length to  $\mathbf{C}_R$ . In this study, the  
284 correlation length is determined based on the empirical covariance of model estimated  
285  $\Delta TWS$ . The covariance function of  $\Delta TWS$  is firstly assumed isotropic, and it is computed  
286 empirically based on the method given in Tscherning and Rapp (1974). The distance where  
287 the maximum value of the variance decreases to half is defined as the correlation length. The  
288 obtained values vary month-to-month, and the mean value of 250 km is used in this study.

289 It is emphasized that the model omission error caused by imperfect modelling of hydrological  
290 process within the LSM is not taken into account in the above description. The omission error  
291 may increase the model covariance and introduce a bias as well. We account for the omission  
292 error by increasing 20% of the model covariance. (i.e., multiplying  $\mathbf{C}_R$  by 1.2). We determine  
293 such omission error based on trial-and-error such that it increases the model error (due to the  
294 omission error) but not exceeds the model error value reported by Dumedah and Walker  
295 (2014). We acknowledge that this is only a simple practical way of accounting for the  
296 omission error into the total model error.

297

## 298 **4.3 Validation data**

### 299 **4.3.1 Satellite soil moisture observation**

300 The satellite observed surface soil moisture data is obtained from the Advanced Microwave  
301 Scanning Radiometer-Earth Observing System (AMSR-E) using the Land Parameter  
302 Retrieval Model (Njoku et al., 2003). The observation is used to validate our estimates of top  
303 soil moisture changes ( $\Delta SM_{top}$ ). The AMSR-E product provides volumetric water content in  
304 the top layer derived from a passive microwave data (from NASA EOS Aqua satellite) and  
305 forward radiative transfer model. In this study, the level 3 product, available daily between  
306 June 2002 and June 2011 at  $0.25^\circ \times 0.25^\circ$  spatial resolution is used (Owe et al., 2008). The  
307 measurements from ascending and descending overpasses are averaged for each frequency  
308 band (C and X). Then, the monthly mean value is computed by averaging the daily data  
309 within a month. To obtain the variation of the surface soil moisture, the long-term mean  
310 between June 2002 and June 2011 is removed from the monthly data. Regarding the different  
311 depth measured in CABLE and AMSR-E, the CDF-matching technique (Reichle and Koster,  
312 2004) is used to reduce the bias between the top soil moisture model and the observation. The  
313 CDF is built using the 2003-2004 data, and it is used for the entire period. There is no  
314 satellite observed or ground measured root zone soil moisture data for meaningful  
315 comparison with our results, particularly at continental scale. Validation of  $\Delta SM_{rz}$  at regional  
316 and continental scales is currently unachievable due to a complete lack of observations at this  
317 spatial scale.

318

### 319 **4.3.2 In-situ groundwater**

320 The in-situ groundwater level from bore measurements are obtained from 2 different ground  
321 observation networks (see Fig. 1). The data in Queensland are obtained from Department of



322 Natural Resources and Mines (DNRM) while the data in Victoria is from Department of  
323 Environment and Primary Industries (DWPI). More than 10,000 measurements are available  
324 from each network, but the data gap and outliers are present. Therefore, the bore  
325 measurement is firstly filtered by removing the sites that present no data or data gap longer  
326 than 30 months during the study period.

327 To obtain the monthly mean value, the hourly or daily data are averaged in a particular  
328 month. The outliers are detected and fixed using the Hampel filter (Pearson, 2005) where the  
329 remaining data gaps are filled using the cubic spline interpolation. To obtain the groundwater  
330 level variation, the long-term mean groundwater level computed between the study period is  
331 removed from the monthly values. The groundwater level variation ( $\Delta L$ ) is then converted to  
332  $\Delta GWS$  using  $\Delta GWS = S_y \cdot \Delta L$ , where  $S_y$  is specific yield. Based on Chen et al. (2016),  $S_y =$   
333 0.1 is used for the Victoria network. Specific yields of Queensland's network have been  
334 found ranging from 0.045 (Rassam et al., 2013) to 0.06 (Welsh 2008), and an averaged  $S_y =$   
335 0.05 is used in this study. Finally, the mean value computed from all data (in each network) is  
336 used to represent the in-situ data of the network.

337

## 338 5. Results

### 339 5.1 Model-only performance

340 We study the model  $\Delta TWS$  changes under different meteorological forcing and land  
341 parameterization. Total 210 estimates of monthly  $TWS$  (sum of  $SM_{top}$ ,  $SM_{rz}$ , and  $GWS$ ) are  
342 obtained between January 2003 and March 2016 from the ensemble run based on 7 different  
343 precipitation inputs. Then, the averaged values of the  $TWS$  estimates are computed from the  
344 30 precipitation-associated ensemble members. This results in 7 sets of monthly mean  $TWS$   
345 estimates from 7 different precipitation data. For each set, the monthly  $\Delta TWS$  is computed by  
346 removing the long-term mean computed between January 2003 and March 2016.

347 The precipitation-based  $\Delta TWS$  are then compared with the GRACE-mascon solution (see  
348 Sect. 3.2) over 10 different Australian basins. The comparison is carried out between January  
349 2003 and March 2016. Due to the availability of the data, the periods used are shorter in cases  
350 of GSWP3, Princeton, and MERRA precipitation (see Table 1). The metric used to evaluate a  
351 goodness of fit between CABLE run and GRACE mascon estimates is the Nash-Sutcliffe (NS)  
352 coefficient (see Eq. (A1)) (Fig. 2).

353 Figure 2 demonstrates CABLE  $\Delta TWS$  varies noticeably by precipitation as well as locations.  
354 The area-weighted average values (see Eq. (A2)) computed from Princeton, GSWP3, and  
355 TRMM yields the model  $\Delta TWS$  reasonably agreeing with GRACE by giving the NS  
356 coefficient greater than 0.45, while MERRA, PERSIANN, and GLDAS show  $NS = \sim 0.3$ . The  
357 less agreement is mainly due to the quality of rainfall estimates over Australia. The NS of  
358 ECMWF is around 0.4.

359 All model ensembles are consistent with the GRACE data over Timor Sea and inner parts of  
360 Australia (e.g., LKE, MRD, NWP) where the NS value can reach as high as 0.9 (see e.g.,  
361 TRMM over TIM). On the contrary, the less agreement is found mostly over the coastal  
362 basins. Very small or even negative NS values indicate the misfit between CABLE and  
363 GRACE mascon solutions, and they are observed over Indian Ocean (see GLDAS), North

364 East Coast (see GSWP3, PERSIANN, TRMM), South East Coast (see MERRA, TRMM),  
365 South West Coast (see GSWP3, GLDAS, MERRA), and South West Plateau (see MERRA).

366 By averaging all  $\Delta TWS$  estimates from seven different precipitation datasets, the mean-  
367 ensemble estimate (MN) delivers the best agreement with GRACE as seen by the highest  
368 average NS value (MN of AVG = 0.55) among all ensembles. Particularly, NS values are  
369 greater than 0.4 in all basins and no negative NS values are presented in MN. In average, it  
370 can be clearly seen that using the mean value (MN) is a viable option to increase the overall  
371 performance of the  $\Delta TWS$  estimates. Therefore, only CABLE MN result will be used in  
372 further analyses. The comparison with the GRGS GRACE solution was also evaluated (not  
373 shown here) and the overall results are similar to Fig. 2.

374

## 375 **5.2 Impact of GRACE on storage estimates**

### 376 **5.2.1 Contribution of GRACE**

377 This section investigates the impact of the GC approach on the estimates of various water  
378 storage components. The  $\Delta TWS$  estimate obtained from the GC approach is demonstrated in  
379 Sect. 5.1, by comparing with the independent GRACE mascon solution. Figure 2 shows the  
380 GC result yields the highest NS values in all basins, outperforming all other CABLE runs. In  
381 average (AVG), the NS value increases by ~35% (0.55 to 0.74) from the MN case. The  
382 similar behaviour is also seen when compared with the GRGS GRACE solution (not shown);  
383 the average NS value increases from 0.50 to 0.74. This is not surprising as the GC approach  
384 uses the fundamental GRACE tracking data as GRACE mascon and GRGS solutions do.  
385 Improvement of NS coefficient indicates merely the successfulness of integrating GRACE  
386 data and the model estimates.

387 Figure 3 shows the GC results of  $\Delta TWS$  as well as  $\Delta SM_{top}$ ,  $\Delta SM_{rz}$ , and  $\Delta GWS$  in different  
388 basins. The monthly time-series and the de-seasonalized time-series are shown. In general,  
389 GRACE tends to increase  $\Delta TWS$  when the model  $\Delta TWS$  (MN) is predicted to be  
390 underestimated (see e.g., LKE, MRD, NWP, SWP, TIM between 2011 and 2012) and by  
391 decrease  $\Delta TWS$  when determined to be overestimated (see all basins between 2008 and  
392 2010). A clear example is seen over Gulf of Carpentaria (Fig. 3d), where CABLE  
393 overestimates  $\Delta TWS$  and produces phase delay between 2008 and 2010. The over estimated  
394 amplitude and phase delay seen in CABLE  $\Delta GWS$  during this above period (Fig. 3c) is  
395 caused by an overestimation of soil and groundwater storage. The positively biased soil and  
396 groundwater storage causes a phase delay by increasing the amount of time required for the  
397 subsurface drainage (baseflow) to reduce to soil and groundwater stores. The overestimation  
398 of water storage is the result of overestimated precipitation or underestimated  
399 evapotranspiration. The amplitude and phase of the water storage estimate are adjusted  
400 toward GRACE observation in the GC approach.

401 The impact of GRACE varies across the individual storage as well as across the geographical  
402 location (climate regime). In general, the major contributors to  $\Delta TWS$  are  $\Delta SM_{rz}$  and  $\Delta GWS$ .  
403 Due to a small store size (only ~2 cm thick),  $\Delta SM_{top}$  contributes only ~2 % to  $\Delta TWS$ . As  
404 such,  $\Delta SM_{rz}$ , and  $\Delta GWS$  have greater variations, which commonly lead to greater uncertainty  
405 compared to  $\Delta SM_{top}$ , and therefore, the stores anticipate greater shares from the GRACE

406 update. This behaviour is seen over all basins where the differences between CABLE-  
407 simulated and GC  $\Delta SM_{rz}$ , and  $\Delta GWS$  estimates are greater (compared to  $\Delta SM_{top}$ ).

408 Furthermore, the impact of GRACE on  $\Delta SM_{rz}$ , and  $\Delta GWS$  is different across the continent.  
409 For example, over central and southern Australia (see e.g., LKE, MRD, NWP, SWP), the dry  
410 climate is responsible for a small amount of groundwater recharge and most of the infiltration  
411 is stored in soil compartments. In this climate condition,  $\Delta SM_{rz}$  amplitude is significantly  
412 larger than  $\Delta GWS$  and it plays a greater role in  $\Delta TWS$ , and consequently, the GRACE  
413 contribution is mostly seen in  $\Delta SM_{rz}$  component. Different behaviour is seen over the  
414 northern Australia (GOC, NEC, TIM) where  $\Delta GWS$  amplitude are greater (~40 % of  $\Delta TWS$ )  
415 compared to other basins (only ~17 % of  $\Delta TWS$ ). This is due to the sufficient amount of  
416 rainfall over the wet climate region, replenishing groundwater recharges and resulting in  
417 greater variability in  $\Delta GWS$ . Therefore, compared to the dry climate basin, the GRACE  
418 contributes to  $\Delta GWS$  over these basins by the larger amount.  
419

### 420 **5.2.2 Impact on long-term trend estimates**

421 The spatial patterns of the long-term trends of water storage changes over January 2003 and  
422 March 2016 are analysed before and after applying the GC approach (Fig. 5). For  
423 comparison, the long-term trends of  $\Delta TWS$  derived from the mascon and GRGS solutions are  
424 also shown (Fig. 5a, 5b). From Fig. 5d, GRACE effectively changes the long-term trend  
425 estimates in most basins in a way the spatial pattern of the  $\Delta TWS$  trend of the GC solution  
426 consistent to the mascon and GRGS solutions, while satisfying the model processes and  
427 keeping the spatial resolution. The trend of  $\Delta SM_{top}$  is insignificant (Fig. 5e) and the GC  
428 approach does not change (Fig. 5f). The largest adjustment is seen in  $\Delta SM_{rz}$  and  $\Delta GWS$   
429 components, to be consistent with the GRACE data in most basins (Fig. 5h, 5j).

430 GRACE shows significant changes in the  $\Delta TWS$  trend estimates particularly over the  
431 northern and western parts of the continent. The model estimates around the Gulf of  
432 Carpentaria basin show a strong negative trend that is inconsistent from the GRACE data. It  
433 is found that underestimated precipitation after 2012 is likely the cause of such an  
434 incompatible negative trend (see Fig. 3d). Applying the GC approach clearly improves the  
435 trend (Fig. 5c vs. 5d). The other example is seen over the western part of the continent (see  
436 rectangular area in Fig. 5c, 5d) where the averaged long-term trend of  $\Delta TWS$  was predicted  
437 to be  $-0.4$  cm/year but changed to be  $-1.2$  cm/year (see also Sect. 5.4) by the GC approach.  
438 The precipitation over the western Australia is understood to be overestimated after 2012,  
439 evidently seen by that the model  $\Delta TWS$  is always greater than the GC solution (see e.g., Fig.  
440 3h, 4d, 4p). The GC approach reveals that the water loss over the western Australia is at least  
441 twice greater than what has predicted by the CABLE model.

442 In addition, the shortage of water storage in the south-eastern part of the continent from the  
443 millennium drought (McGrath et al., 2012) has been recovered (seen as a positive water  
444 storage trend in Fig. 5) after the rainfall between 2009 and 2012, while the western part is  
445 still drying out (seen as negative trends). The trend estimates in terms of mass change is  
446 discussed in more detail in Sect. 5.4.  
447

### 448 **5.2.3 Reduction of uncertainty**

449 Influenced by climate pattern, the uncertainty of water storage estimates significantly varies  
450 across Australia. The uncertainty of the model estimate is computed from the variability  
451 induced by different precipitation and model parameters while the uncertainty of GC solution  
452 is computed using Eq. (13). As expected, larger uncertainties are observed in  $\Delta SM_{rz}$  and  
453  $\Delta GWS$  than in  $\Delta SM_{top}$  (an order of magnitude smaller) since  $\Delta SM_{top}$  is smaller than others  
454 (Fig. 6). Over the wet basins, larger amplitude of the water storage leads to larger uncertainty,  
455 seen over Gulf of Carpentaria, North East Coast, South East Coast, and Timor Sea where the  
456 CABLE-simulated  $\Delta TWS$  uncertainty is approximately 28 % larger than other basins. The  
457 smaller uncertainty is found over the dry regions (e.g., LKE, SWP). In most basins, the  
458 uncertainty of  $\Delta SM_{rz}$  is larger than the  $\Delta GWS$ , except the wet basins (e.g., GOC, NEC, TIM)  
459 where the greater groundwater recharge leads to a larger uncertainty of  $\Delta GWS$ .

460 Figure 6 demonstrates how much the formal error of each of storage components is reduced  
461 by the GC approach. Overall, the estimated CABLE uncertainties averaged over all basins  
462 (AVG) are 0.2, 4.0, 4.0, and 5.7 cm for  $\Delta SM_{top}$ ,  $\Delta SM_{rz}$ ,  $\Delta GWS$ , and  $\Delta TWS$ , respectively.  
463 With the GC approach, the uncertainties of  $\Delta SM_{top}$ ,  $\Delta SM_{rz}$ ,  $\Delta GWS$ , and  $\Delta TWS$  decrease by  
464 approximately 26%, 35%, 39%, and 37%, respectively.

465 It is worth mentioning that the model uncertainty is mainly influenced by the meteorological  
466 forcing data. The uncertainty of precipitation derived from seven different precipitation  
467 products is shown in Fig. 6e. The spatial pattern of the precipitation uncertainty is correlated  
468 with the uncertainty of water storage estimates. The larger water storage uncertainty is  
469 deduced from the larger precipitation uncertainty. The quality of precipitation forcing data is  
470 found to be an important factor to determine the accuracy of water storage computation.  
471

## 472 **5.3 Comparison with independent data**

### 473 **5.3.1 Soil moisture**

474 The  $\Delta SM_{top}$  estimates are compared with the AMSR-E derived soil moisture. The processing  
475 of AMSR-E data is described in Sect 4.3.1. The performance is assessed using Nash-Sutcliffe  
476 coefficients, given in Table 3. In general, CABLE (MN) shows a good performance in the top  
477 soil moisture simulation showing NS value of  $>0.4$  for most of the basins. The top soil  
478 moisture estimate shows slightly better agreement with the C-band measurement of the  
479 AMSR-E product. This is likely caused by the greater emitting depth of the C-band  
480 measurement ( $\sim 1$  cm), which is closer to the depth of the top soil layer ( $\sim 2$  cm) used in this  
481 study (Njoku et al., 2003).

482 The GC approach leads to a small bit of improvement of the top soil estimate consistently  
483 from C- and X-band measurements and from all basins. No degradation of the NS value is  
484 observed in the GC solutions. The largest improvement is seen over LKE and NEC, where  
485 NS increases by 10 – 15%. For other regions, the change in the NS coefficient may be  
486 incremental.  
487

### 488 **5.3.2 Groundwater**

489 The  $\Delta GWS$  estimates from the model and the GC method are compared with the in situ data  
490 obtained from 2 different ground networks in Queensland and Vitoria. For each network, all

491  $\Delta GWS$  data inside the groundwater network boundary (see polygons in Fig. 1) are used to  
492 compute the average  $\Delta GWS$  time series. From the comparison given in Fig. 7, it is found that  
493 the GC solutions of  $\Delta GWS$  follows the overall inter-annual pattern of CABLE but with a  
494 considerably larger amplitude. This results in a better agreement with the in situ  $\Delta GWS$  data  
495 seen from both networks. The NS coefficient of  $\Delta GWS$  between the estimates and the in situ  
496 data are given in Table 4. The CABLE  $\Delta GWS$  performs significantly better in Queensland  
497 (NS =  $\sim 0.5$ ) than Victoria (NS =  $\sim 0.3$ ). Significant improvement is found from the GC  
498 solutions in both networks, where the NS value increases from 0.5 to 0.6 ( $\sim 22\%$ ) in  
499 Queensland and from 0.3 to 0.6 ( $\sim 85\%$ ) in Victoria. Even greater improvement is seen when  
500 the inter-annual patterns are compared. The NS value increase from 0.5 to 0.7 ( $\sim 32\%$ ), and  
501 0.4 to 0.8 ( $\sim 93\%$ ) in Queensland and Victoria, respectively.

502 The comparison of the long-term trend of  $\Delta GWS$  is also evaluated. The estimated trends in  
503 Queensland and Victoria are given in Table 4. Beneficially from the GC approach, the  $\Delta GWS$   
504 trend is improved by approximately 20% (from 0.4 to 0.6, compared to 1.6 cm/year) in  
505 Queensland. Increasing of  $\Delta GWS$  is mainly influenced by the large amount of rainfall during  
506 the 2009 – 2012 La Niña episodes (see Fig. 7a). In Victoria, significant improvement of  
507  $\Delta GWS$  trend by about 76% (from 0.1 to  $-0.2$ , compared to  $-0.3$  cm/year) is observed.  
508 Similar improvement of long-term trend estimates is seen in de-seasonalized time series  
509 (improves by  $\sim 15\%$  in Queensland and by  $\sim 74\%$  in Victoria). Decreasing of  $\Delta GWS$  in  
510 Victoria is mainly due to the highly-demanded groundwater consumption by agriculture and  
511 domestic activities (van Dijk et al., 2007; Chen et al., 2016). As the groundwater  
512 consumption is not parameterized in CABLE, the decreasing of  $\Delta GWS$  estimate cannot  
513 properly captured in the model simulation. Applying GC approach effectively reduces the  
514 model deficiency and improves the quality of the groundwater estimations.

515

#### 516 **5.4 Assessment of mass variation in the past 13 years**

517 Australia experiences significant climate variability; for example the millennium drought  
518 starting from late '90 (Van Dijk et al., 2013) and extremely wet condition during several La  
519 Niña episodes (Trenberth 2012; Han 2017). These periods are referred as “Big Dry” and “Big  
520 Wet” (Ummenhofer et al., 2009; Xie et al., 2016). To understand the total water storage  
521 (mass) variation influenced by these two distinct climate variabilities, the water storage  
522 change obtained from the GC approach during Big Dry and Big Wet is separately  
523 investigated over 10 basins. The time window between January 2003 and December 2009 is  
524 defined as the Big Dry period while between January 2010 and December 2012 is defined as  
525 the Big Wet period following Xie et al. (2016). In each period, the long-term trends of GC  
526 estimates of  $\Delta TWS$ ,  $\Delta SM_{top}$ ,  $\Delta SM_{rz}$ , and  $\Delta GWS$  are firstly calculated. Then, the total water  
527 storage variation (in meter) is simply obtained by multiplying the long-term trend (in m/year)  
528 with the number of years in the specific period, 7 years for Big Dry and 3 years for Big Wet.  
529 To obtain the mass variation, the water storage variation is multiplied by the area of the basin  
530 and the density of water ( $1000 \text{ kg/m}^3$ ). The estimated mass variations during Big Dry and Big  
531 Wet are displayed in Fig. 8. The long-term mass variation of the entire period (January 2003  
532 – March 2016) is also shown.

533 During Big Dry (2003 – 2009), a significant loss of total storage (40 – 60 Gton over 7 years)  
534 is observed over LKE, MRD, NWP, and SWP basins. The largest groundwater loss of  $>20$

535 Gton is found from LKE and MRD. No significant change is observed over the tropical  
536 climate regions (e.g., GOC, NEC). The mass loss mostly occurs in the root zone and  
537 groundwater compartments where the sum of  $\Delta SM_{rz}$  and  $\Delta GWS$  explains more than 90% of  
538 the  $\Delta TWS$  value. The mass loss is also observed in  $\Delta SM_{top}$  but >10 times smaller than  
539  $\Delta SM_{rz}$  and  $\Delta GWS$ .

540 During Big Wet (2010 – 2012), the basins like LKE, MRD and TIM exhibit the significant  
541 total storage gain of >100 Gton. The gain is particularly larger in  $\Delta SM_{rz}$  over the basins that  
542 experienced the significant loss during Big Dry. For example, over LKE and MRD, the gain  
543 of  $\Delta SM_{rz}$  is approximately 2 – 3 times greater than  $\Delta GWS$ . It implies that most of the  
544 infiltration (from the 2009 – 2012 La Niña rainfall) is stored as soil moisture through the long  
545 drought period, and that the groundwater recharge is secondary to the  $\Delta SM_{rz}$  increase.

546 The opposite behaviour is observed over the basins (such as NEC and GOC) that experienced  
547 mass gain during Big Dry. The water storage gain is greater in  $\Delta GWS$  compared to  $\Delta SM_{rz}$ . In  
548 NEC,  $\Delta GWS$  gain is ~8 times larger than  $\Delta SM_{rz}$  during Big Wet. The soil compartment may  
549 be saturated during Big Dry and additional infiltration from the Big Wet precipitation leads to  
550 an increased groundwater recharge. The  $\Delta SM_{rz}$  loss observed over GOC is simply caused by  
551 the timing selection of Big Wet period, which ends earlier (~2011) in GOC than in other  
552 basins. The  $\Delta SM_{rz}$  gain becomes ~26 Gton if the Big Wet period is defined as 2008 – 2011.  
553 During the post-Big Wet period (2012 and afterwards), the decreasing trend of water storage  
554 is observed from all basins (see Fig. 3, 4). This is mainly caused by the decrease in  
555 precipitation after 2012 and by gradual water loss through evapotranspiration (Fasullo et al.,  
556 2013).

557 The overall water storage change in the last 13 years demonstrates that the severe water loss  
558 from most basins during Big Dry (the millennium drought) is balanced with the gain during  
559 Big Wet (the La Niña). The negative  $\Delta TWS$  estimated during Big Dry becomes positive in  
560 LKE, MRD, and SEC and less negative in TIM, and the greatest gain is observed from NEC  
561 by ~50 Gton during 13 year-period (see Fig. 8c). However, the water mass loss is still  
562 detected over the western basins (e.g., IND, NWP, SWP, SWC), and their magnitudes are  
563 even larger than the mass loss during Big Dry. For example, the greatest  $\Delta TWS$  loss of ~79  
564 Gton is observed over NWP, which is ~25 Gton greater than the loss during Big Dry (see Fig.  
565 8a and 8c). The basin is less affected by the La Niña, and the rainfall during Big Wet is  
566 clearly inadequate to support the water storage recovery in the basin. Rainfall deficiency also  
567 reduces the groundwater recharge, resulting in even more decreasing of  $\Delta GWS$ , compared to  
568 the Millennium Drought period (see Fig. 8j and 8l). The continual decrease in water storage  
569 over western basins is likely caused by the interaction of complex climate patterns like El  
570 Niño Southern Oscillation, Indian Ocean Dipole, and Southern Annular Mode cycles  
571 (Australian Bureau of Meteorology, 2012; Xie et al., 2016).

572

## 573 **5.5 Comparison of GC approach with alternatives**

574 The simplest approach to estimate  $\Delta GWS$  is to subtract the model soil moisture component  
575 from GRACE  $\Delta TWS$  data, without considering uncertainty in the model output, as used in  
576 Rodell et al. (2009) and Famiglietti et al. (2011). This method is called Approach 1 (App 1).  
577 In Approach 2 (App 2) as in Tangdamrongsub et al. (2017), by accounting for the uncertainty

578 of model outputs and GRACE data, the water storage states are updated through a Kalman  
 579 filter:

$$580 \quad \hat{\mathbf{h}}_R = \tilde{\mathbf{h}}_R + \mathbf{H}\mathbf{C}_R^T(\mathbf{H}\mathbf{R}\mathbf{H}^T + \mathbf{C}_R)^{-1}(\mathbf{b} - \mathbf{H}\tilde{\mathbf{h}}_R) \quad (20)$$

581 where  $\tilde{\mathbf{h}}_R$ ,  $\mathbf{H}$ ,  $\mathbf{C}_R$  are described in Sect. 2,  $\mathbf{b}$  is an observation vector containing GRACE-  
 582 derived  $\Delta TWS$ , and  $\mathbf{R}$  is an error variance-covariance matrix of the observation. The  
 583 GRACE-derived  $\Delta TWS$  and its error information is obtained from the mascon solution. The  
 584 matrix  $\mathbf{R}$  is a (diagonal) error variance matrix since no covariance information is given in the  
 585 mascon product. Note that the model uncertainty remains the same as in GC approach (Sect.  
 586 4.2). The different results from App1 and App2 are mainly attributed to the different estimates  
 587 of the uncertainty.

588 The  $\Delta GWS$  estimates from App1, App2 and GC in Queensland and Victoria are shown in  
 589 Fig. 9. It is clearly seen that  $\Delta GWS$  from App1 are overestimated while the one from App2  
 590 fits the ground data significantly better. This behaviour was also seen in Tangdamrongsub et  
 591 al. (2017) that the water storage estimates tend to be overestimated when error components  
 592 such as spatial correlation error were neglected as in App1.  $\Delta GWS$  from App2 shows clear  
 593 improvements in terms of NS coefficients in both networks. Considering the de-seasonalized  
 594  $\Delta GWS$  estimates, in Queensland, the trend increases from  $0.39 \pm 0.03$  to  $0.42 \pm 0.03$  cm/year  
 595 (improves by 1.5%), and the NS value increases from 0.46 to 0.53. In Victoria, the trend  
 596 decreases from  $0.73 \pm 0.10$  to  $0.46 \pm 0.05$  cm/year (improves by 27%), and the NS value  
 597 increases from  $-0.89$  to 0.30. Although App2 is not yet as good as the GC solution based on  
 598 the most comprehensive error propagation, this simple test demonstrates an important of  
 599 considering the uncertainty. The reason of App2 being less accurate than GC is likely due to  
 600 too simplified error information implemented in App2.

601

## 602 **6. Conclusion**

603 This study presents an approach of combining the raw GRACE observation with model  
 604 simulation to improve water storage estimates over Australia. Distinct from other methods,  
 605 we exploit the fundamental GRACE satellite tracking data and the full data error variance-  
 606 covariance information to avoid alteration of signal and measurement error information  
 607 present in higher level data products.

608 We compare groundwater storage estimates from GC approach and two other approaches,  
 609 subject to inclusion of GRACE uncertainty in  $\Delta GWS$  calculation. Validating three results of  
 610  $\Delta GWS$  against the in situ groundwater data, we find that the GC approach delivers the most  
 611 accurate groundwater estimate, followed by the approach based on incomplete information of  
 612 GRACE's data error. The poorest estimate of groundwater storage is seen when the GRACE  
 613 uncertainty is completely ignored. This confirms the critical value of using the complete  
 614 GRACE signal and error information at the raw data level.

615 The analysis of water storage change between 2003 and 2016 reveals that half of the  
 616 continent (5 out of 10 basins) is still not fully recovered from the Millennium Drought. The  
 617 TWS decrease in Western Australia has been most characteristic and the GC approach finds  
 618 that the water loss mainly occur in groundwater layer. Rainfall inadequacy is attributed to the

619 continual dry condition, leading to a greater decreasing of groundwater recharge and storage  
620 over Western Australia.

621 The land surface model we used is deficient in anthropogenic groundwater consumption. The  
622 model calibration will never help and the groundwater consumption must be brought in by  
623 external sources. On the contrary, the statistical approach like our GC approach may be  
624 useful to fill in the missing component and lead to a more comprehensive water storage  
625 inventory.

626 However, it is difficult to constrain different water storage components by only using total  
627 storage observation like GRACE. In addition, it is challenging to improve surface soil  
628 moisture varying rapidly in time, using a monthly mean GRACE observation. Tian et al.  
629 (2017) utilized the satellite soil moisture observation from the Soil Moisture and Ocean  
630 Salinity (SMOS, Kerr et al., 2001) in addition to GRACE data for their data assimilation and  
631 showed a clear improvement in the top soil moisture estimate. The GC approach with  
632 complementary observations at higher temporal resolution should be considered particularly  
633 to enhance the surface soil moisture computation.

634 Finally, the GC approach can be simply extended for GRACE data assimilation. Assimilating  
635 the raw GRACE data into land surface models like CABLE enables the model state and  
636 parameter to be adjusted with the realistic error information, allowing reliable storage  
637 computation. The GC data assimilation will be developed in our future study.

638

### 639 **Acknowledgement**

640 This work was funded by NASA projects on GRACE and GRACE Follow-On missions and  
641 partly by Australian Research Council (DP160104095). MD was supported by ARC Centre  
642 of Excellence for Climate Systems Science. HK was supported by Japan Society for the  
643 Promotion of Science KAKENHI (16H06291). We thank Torsten Mayer-Gürr for GRACE  
644 data products in the form of the least-squares normal equations. We also thank three  
645 anonymous reviewers for helping us improve the manuscript.

646



647 **Appendix: Nash-Sutcliff coefficient and area-weighted average**

648 Nash-Sutcliff coefficient (NS) is computed as follows:

649 
$$NS = 1 - \frac{\sum_{i=1}^N (\mathbf{y}_i - \hat{\mathbf{x}}_i)^2}{\sum_{i=1}^N (\mathbf{y}_i - \bar{\mathbf{y}})^2} \quad (\text{A1})$$

650 where  $\mathbf{y}$  is an observation vector,  $\bar{\mathbf{y}}$  is the mean of the observation,  $\hat{\mathbf{x}}$  is a vector containing  
651 the simulated result,  $i$  is the index of observation, and  $N$  is the number of observation.

652 Area-weighted average ( $\bar{Z}$ ) is compute as follows:

653 
$$\bar{Z} = \frac{\sum_{j=1}^M w_j \bar{z}_j}{\sum_{j=1}^M w_j} \quad (\text{A2})$$

654 where  $w$  is the area size,  $\bar{z}$  is the mean value inside the considered area,  $j$  is the area index,  
655 and  $M$  is the number of considered area.

656

657 **References**

- 658 Australian Bureau of Meteorology (2012) Record-breaking La Niña events: An analysis of  
659 the La Niña life cycle and the impacts and significance of the 2010–11 and 2011–12 La Niña  
660 events in Australia, National Climate Centre, Bureau of Meteorology,  
661 <http://www.bom.gov.au/climate/enso/history/La-Nina-2010-12.pdf> (last accessed: 5 January  
662 2017).
- 663 Bettadpur, S.: CSR Level-2 Processing Standards Document for Product Release 05, GRACE  
664 327-742, Center for Space Research, The University of Texas at Austin, 2012.
- 665 Chen, J. L., Wilson, C. R., Tapley, B. D., Scanlon, B., Güntner, A.: Long-term groundwater  
666 storage change in Victoria, Australia from satellite gravity and in situ observations, *Glob.*  
667 *Planet. Change*, 139, 56–65, doi: <http://dx.doi.org/10.1016/j.gloplacha.2016.01.002>, 2016.
- 668 Decker, M.: Development and evaluation of a new soil moisture and runoff parameterization  
669 for the CABLE LSM including subgrid-scale processes, *J. Adv. Model. Earth Syst.*, 7, 1788–  
670 1809, doi:10.1002/2015MS000507, 2015.
- 671 Dee, D. P., Uppala, S. M., Simmons, A. J., Berrisford, P., Poli, P., Kobayashi, S., Andrae, U.,  
672 Balmaseda, M. A., Balsamo, G., Bauer, P., Bechtold, P., Beljaars, A. C. M., van de Berg, L.,  
673 Bidlot, J., Bormann, N., Delsol, C., Dragani, R., Fuentes, M., Geer, A. J., Haibergger, L.,  
674 Healy, S. B., Hersbach, H., Hólm, E. V., Isaksen, L., Kállberg, P., Köhler, M., Matricardi,  
675 M., McNally, A. P., Monge-Sanz, B. M., Morcrette, J. J., Park, B. K., Peubey, C., de Rosnay,  
676 P., Tavolato, C., Thépaut, J. N., and Vitart, F.: The ERA-Interim reanalysis: configuration  
677 and performance of the data assimilation system. *Quarterly Journal of the Royal*  
678 *Meteorological Society*, 137, 553–597, doi:10.1002/qj.828, 2011.
- 679 Dumedah, G., and Walker, J. P.: Intercomparison of the JULES and CALBE land surface  
680 models through assimilation of remote sensed soil moisture in southeast Australia, *Adv. Wat.*  
681 *Res.*, 74, 231 – 244, doi:[hmattp://dx.doi.org/10.1016/j.advwatres.2014.09.011](http://dx.doi.org/10.1016/j.advwatres.2014.09.011), 2014.
- 682 Eicker, A., Schumacher, M., Kusche, J., Döll, P., and Müller Schmied, H.: Calibration data  
683 assimilation approach for integrating GRACE data into the WaterGAP Global Hydrology  
684 Model (WGHM) using an Ensemble Kalman Filter: First Results, *Surv. Geophys.*, 35(6),  
685 1285-1309, doi:10.1007/s10712-014-9309-8, 2014.
- 686 Evensen, G.: The ensemble Kalman filter: Theoretical formulation and practical  
687 implementation, *Ocean Dyn.*, 53(4), 343-367, doi:10.1007/S10236-003-0036-9, 2003.
- 688 Famiglietti, J. S., Lo, M., Ho, S. L., Bethune, J., Anderson, K. J., Syed, T. H., Swenson, S.  
689 C., de Linage, C. R., and Rodell, M.: Satellites measure recent rates of groundwater depletion  
690 in California’s Central Valley, *Geophys. Res. Lett.*, 38, L03403, doi:10.1029/2010GL046442,  
691 2011.
- 692 Fasullo, J. T., Boening, C., Landerer, F. W., and Nerem, R. S.: Australia’s unique influence  
693 on global sea level in 2010–2011, *Geophys. Res. Lett.*, 40, 4368–4373,  
694 doi:10.1002/grl.50834, 2013.
- 695 Forman, B. A., Reichle, R. H., and Rodell, M.: Assimilation of terrestrial water storage from  
696 GRACE in a snow-dominated basin, *Water Resour. Res.*, 48, W01507,  
697 doi:10.1029/2011WR011239, 2012.

698 Forootan, E., Safari, A., Mostafaie, A., Schumacher, M., Delavar, M., and Awange, J. L.:  
699 Large-Scale Total Water Storage and Water Flux Changes over the Arid and Semiarid Parts  
700 of the Middle East from GRACE and Reanalysis Products, *Surv. Geophys.*, 38:591-615,  
701 doi:10.1007/s10712-016-9403-1, 2017.

702 Giroto, M., De Lannoy, G. J. M., Reichle, R. H., and Rodell, M.: Assimilation of gridded  
703 terrestrial water storage observations from GRACE into a land surface model, *Water Resour.*  
704 *Res.*, 52(5), 4164–4183, doi:10.1002/2015WR018417, 2016.

705 Hamill, T. M., Whitaker, J. S., and Snyder, C.: Distance-Dependent Filtering of Background  
706 Error Covariance Estimates in an Ensemble Kalman Filter, *Mon. Weather Rev.*, 129, 2776–  
707 2790, 2001.

708 Han, S.-C.: Elastic deformation of the Australian continent induced by seasonal water cycles  
709 and the 2010-11 La Niña determined using GPS and GRACE, *Geophys. Res. Lett.*, 44, doi:  
710 10.1002/2017GL072999, 2017.

711 Huffman, G. J., Adler, R. F., Bolvin, D. T., Gu, G., Nelkin, E. J., Bowman, K. P., Hong, Y.,  
712 Stocker, E. F., and Wolf, D. B.: The TRMM multisatellite precipitation analysis (TMPA):  
713 Quasi-global, multiyear, combined-sensor precipitation estimates at fine scales, *J.*  
714 *Hydrometeor.*, 8, 38–55, doi:10.1175/JHM560.1, 2007.

715 Jekeli, C.: Alternative methods to smooth the Earth’s gravity field, Rep., 327, Dept. of Geod.  
716 Sci. and Surv., Ohio State Univ., Columbus, 1981.

717 Kerr, Y. H., Waldteufel, P., Wigneron, J.-P., Martinuzzi, J.-M., Font, J., and Berger, M.: Soil  
718 moisture retrieval from space: The soil moisture and ocean salinity (SMOS) mission, *IEEE*  
719 *Trans. Geosci. Remote Sens.*, 39(8), 1729–1735, 2001.

720 Lambert, A., Huang, J., van der Kamp, G., Henton, J., Mazzotti, S., James, T. S., Courtier,  
721 N., and Barr, A. G.: Measuring water accumulation rates using GRACE data in areas  
722 experiencing glacial isostatic adjustment: The Nelson River basin, *Geophys. Res. Lett.*, 40,  
723 6118–6122, doi:10.1002/2013GL057973, 2013.

724 Landerer, F. W., and Swenson, S. C.: Accuracy of scaled GRACE terrestrial water storage  
725 estimates, *Water Resour. Res.*, 48, W04531, doi:10.1029/2011WR011453, 2012.

726 Leblanc, M., Tweed, S., Van Dijk, A., Timbal, B.: A review of historic and future  
727 hydrological changes in the Murray-Darling Basin, *Global and Planetary Change*, 80 – 81,  
728 226 – 246, doi:10.1016/j.gloplacha.2011.10.012, 2012.

729 Lemoine, J. M., Bourgogne, S., Bruinsma, S., Gégout, P., Reinquin, F., Biancale R.: GRACE  
730 RL03-v2 monthly time series of solutions from CNES/GRGS, EGU2015-14461, EGU  
731 General Assembly 2015, Vienna, Austria, 2015.

732 Mayer-Gürr, T., Behzadpour, S., Ellmer, M., Kvas, A., Klinger, B., Zehentner, N.: ITSG-  
733 Grace2016 - Monthly and Daily Gravity Field Solutions from GRACE. GFZ Data Services.  
734 <http://doi.org/10.5880/icgem.2016.007>, 2016.

735 Mayer-Gürr T., Pail R., Gruber T., Fecher T., Rexer M., Schuh W.-D., Kusche J., Brockmann  
736 J.-M., Rieser D., Zehentner N., Kvas A., Klinger B., Baur O., Höck E., Krauss S., Jäggi A.:  
737 The combined satellite gravity field model GOCO05s, EGU 2015, Vienna, 2015.

738 McGrath, G. S., Sadler, R., Fleming, K., Tregoning, P., Hinz, C., and Veneklaas, E. J.:  
739 Tropical cyclones and the ecohydrology of Australia's recent continental-scale drought,  
740 *Geophys. Res. Lett.*, 39, L03404, doi:10.1029/2011GL050263, 2012.

741 Njoku, E. G., Jackson, T. L., Lakshmi, V., Chan, T., Nghiem, S. V.: Soil Moisture Retrieval  
742 from AMSR-E, *IEEE T. Geosci. Remote*, 41 (2): 215-229, 2003.

743 Owe, M., de Jeu, R., Holmes, T.: Multisensor historical climatology of satellite-derived global  
744 land surface moisture, *J. Geophys. Res.*, 113, F01002, 17 pp., doi:10.1029/2007JF000769,  
745 2008.

746 Pearson, E. K.: Mining imperfect data: Dealing with contamination and incomplete records,  
747 ProSanos Corporation, Harrisburg, Pennsylvania, ISBN: 978-0-89871-582-8, doi:  
748 <http://dx.doi.org/10.1137/1.9780898717884>, 2005.

749 Rassam, D. W., Peeters, L., Pickett, T., Jolly, I., Holz, L.: Accounting for  
750 surface-groundwater interactions and their uncertainty in river and groundwater models: A  
751 case study in the Namoi River, Australia, *Environ. Modell. Softw.*, 50, 108-119,  
752 <http://dx.doi.org/10.1016/j.envsoft.2013.09.004>, 2013.

753 Reichle, R. H., and Koster, R. D.: Bias reduction in short records of satellite soil moisture,  
754 *Geophys. Res. Lett.*, 31, L19501, doi:10.1029/2004GL020938, 2004.

755 Rienecker, M. M., Suarez, M. J., Gelaro R, Todling R, Bacmeister J, Liu E, Bosilovich MG,  
756 Schubert SD, Takacs L, Kim G-K, Bloom S, Chen J, Collins D, Conaty A, da Silva A, Gu W,  
757 Joiner J, Koster RD, Lucchesi R, Molod A, Owens T, Pawson S, Pegion P, Redder CR,  
758 Reichle R, Robertson FR, Ruddick AG, Sienkiewicz M, Woollen J. 2011. MERRA—NASA's  
759 Modern-Era Retrospective Analysis for Research and Applications. *J. Climate*, DOI:  
760 10.1175/JCLI-D-11-00015.1.

761 Rietbroek, R., Fritsche, M., Brunnabend, S.-E., Daras, I., Kusche, J., Schröter, J., Flechtner,  
762 F., and Dietrich, R.: Global surface mass from a new combination of GRACE, modelled OBP  
763 and reprocessed GPS data, *J. Geodyn.*, 59 - 60:64 - 71, doi:10.1016/j.jog.2011.02.003, 2012.

764 Rodell, M., Houser, P. R., Jambor, U., Gottschalck, J., Mitchell, K., Meng, C. J., Arsenault,  
765 K., Cosgrove, B., Radakovich, J., Bosilovich, M., Entin, J. K., Walker, J. P., Lohmann, D.,  
766 and Toll, D.: The global land data assimilation system, *Bull. Amer. Meteor. Soc.*, 85(3), 381–  
767 394, 2004.

768 Rodell, M., Velicogna, I., Famiglietti, J. S.: Satellite-based estimates of groundwater  
769 depletion in India, *Nature*. 460, 999-1002, doi:10.1038/nature08238, 2009.

770 Sakumura, C., Bettadpur, S., and Bruinsma, S.: Ensemble prediction and intercomparison  
771 analysis of GRACE time-variable gravity field models, *Geophys. Res. Lett.*, 41, 1389–1397,  
772 doi:10.1002/2013GL058632, 2014.

773 Schmeer, M., Schmidt, M., Bosch, W., and Seitz, F.: Separation of mass signals within  
774 GRACE monthly gravity field models by means of empirical orthogonal functions, *J.*  
775 *Geodyn.*, 59 - 60:124 - 132, doi:10.1016/j.jog.2012.03.001, 2012.

776 Sheffield, J., Goteti, G., and Wood, E. F.: Development of a 50-yr high-resolution global  
777 dataset of meteorological forcings for land surface modeling, *J. Climate*, 19 (13), 3088-3111,  
778 2005.

779 Schumacher, M., Kusche, J., and Döll, P.: A Systematic Impact Assessment of GRACE Error  
780 Correlation on Data Assimilation in Hydrological Models, *J. Geod.*, 90(6), 537–559.  
781 doi:10.1007/s00190-016-0892-y, 2016.

782 Sorooshian, S., Hsu, K., Gao, X., Gupta, H. V., Imam, B., and Braithwaite, D.: Evaluation of  
783 PERSIANN System Satellite-Based Estimates of Tropical Rainfall, *Bulletin of the American*  
784 *Meteorological Society*, Vol. 81, No. 9, 2035-2046, 2000.

785 Swenson, S. C.: GRACE monthly land water mass grids NETCDF RELEASE 5.0. Ver. 5.0.  
786 PO.DAAC, CA, USA, <http://dx.doi.org/10.5067/TELND-NC005>, 2012. (last accessed: 5  
787 January 2017).

788 Swenson, S. and Wahr, J.: Post-processing removal of correlated errors in GRACE data,  
789 *Geophys. Res. Lett.*, 33(L08402), doi:10.1029/2005GL025285, 2006.

790 Tangdamrongsub, N., Ditmar, P. G., Steele-Dunne, S. C., Gunter, B. C., Sutanudjaja, E. H.  
791 (2016) Assessing total water storage and identifying flood events over Tonlé Sap basin in  
792 Cambodia using GRACE and MODIS satellite observations combined with hydrological  
793 models, *Remote Sens. Environ.*, 181, 162–173,  
794 doi:<http://dx.doi.org/10.1016/j.rse.2016.03.030>.

795 Tangdamrongsub, N., Steele-Dunne, S. C., Gunter, B. C., Ditmar, P. G., and Weerts, A. H.:  
796 Data assimilation of GRACE terrestrial water storage estimates into a regional hydrological  
797 model of the Rhine River basin, *Hydrol. Earth Syst. Sci.*, 19, 2079–2100, doi:10.5194/hess-  
798 19-2079-2015, 2015.

799 Tangdamrongsub, N., Steele-Dunne, S. C., Gunter, B. C., Ditmar, P. G., Sutanudjaja, E. H.,  
800 Xie, T, Wang, Z.: Improving estimates of water resources in a semi-arid region by  
801 assimilating GRACE data into the PCR-GLOBWB hydrological model, *Hydrol. Earth Syst.*  
802 *Sci.*, 21, 2053 – 2074, doi:10.5194/hess-21-2053-2017, 2017.

803 Tian, S., Tregoning, P., Renzullo, L. J., van Dijk, A. I. J. M., Walker, J. P., Pauwels, V. R. N.,  
804 Allgeyer, S.: Improved water balance component estimates through joint assimilation of  
805 GRACE water storage and SMOS soil moisture retrievals, *Water Resour. Res.*, 53,  
806 doi:10.1002/2016WR019641, 2017.

807 Trenberth, K. E.: Framing the way to relate climate extremes to climate change, *Climatic*  
808 *Change*, 115 283–290 , doi:10.1007/s10584-012-0441-5, 2012.

809 Tscherning, C. C. and Rapp R. H.: Closed covariance expressions for gravity anomalies,  
810 geoid undulations, and deflections of the vertical implied by anomaly degree variance  
811 models, Rep. 208, Dep. of Geod. Sci. and Surv., Ohio State Univ., Columbus, 1974.

812 Ukkola, A. M., Pitman, A. J., Decker, M., De Kauwe, M. G., Abramowitz, G., Kala, J., and  
813 Wang, Y.-P.: Modelling evapotranspiration during precipitation deficits: identifying critical  
814 processes in a land surface model. *Hydrol. Earth Syst. Sci.*, 20, 2403–2419, doi:10.5194/hess-  
815 20-2403-2016, 2016.

816 Van Dijk, A., Beck, H. E., Crosbie, R. S., De Jeu, E. A. M., Liu, Y. Y., Podger, G. M.,  
817 Timbal, B., Viney, N. R: The Millennium Drought in southeast Australia (2001–2009):  
818 Natural and human causes and implications for water resources, ecosystems, economy, and  
819 society, *Water Resour. Res.*, 49 (2), 1040 - 1057, doi:10.1002/wrcr.20123, 2013.

820 Van Dijk, A., Podger, G., Kirby, M.: Integrated water resources management in the Murray-  
821 Darling Basin. In: Schumann, A., Pahlow, M. (Eds.), *Increasing demands on decreasing*  
822 *supplies, in Reducing the Vulnerability of Societies to Water Related Risks at the Basin*  
823 *Scale*, IAHS Publ. 24–30, 2007.

824 Voss, K. A., Famiglietti, J. S., Lo, M., de Linage, C., Rodell, M., and Swenson, S. C.:  
825 Groundwater depletion in the Middle East from GRACE with implications for transboundary  
826 water management in the Tigris-Euphrates-Western Iran region, *Water Resour. Res.*, 49,  
827 doi:10.1002/wrcr.20078, 2013.

828 Wahr, J., Molenaar, M., and Bryan, F.: Time variability of the Earth's gravity field:  
829 Hydrological and oceanic effects and their possible detection using GRACE, *J. Geophys.*  
830 *Res.*, 103(B12), 30205–30229, 1998.

831 Wahr, J., Swenson, S., and Velicogna, I.: Accuracy of GRACE mass estimates, *Geophys.*  
832 *Res. Lett.*, 33, L06401, doi:10.1029/2005GL025305, 2006.

833 Watkins, M. M., Wiese, D. N., Yuan, D.-N., Boening, C., and Landerer, F. W.: Improved  
834 methods for observing Earth's time variable mass distribution with GRACE using spherical  
835 cap mascons, *J. Geophys. Res. Solid Earth*, 120, 2648–2671, doi:10.1002/2014JB011547,  
836 2015.

837 Weerts, A. H. and El Serafy G. Y. H.: Particle filtering and ensemble Kalman filtering for  
838 state updating with hydrological conceptual rainfall-runoff models, *Water Resour. Res.*, 42,  
839 W09403, doi:10.1029/2005WR004093, 2006.

840 Welsh, W.D.: Water balance modelling in Bowen, Queensland, and the ten iterative steps in  
841 model development and evaluation, *Environ. Modell. Softw.*, 23 (2), 195-205, 2008.

842 Wiese, D. N., Landerer, F. W., and Watkins, M. M.: Quantifying and reducing leakage errors  
843 in the JPL RL05M GRACE mascon solution, *Water Resour. Res.*, 52, 7490–7502,  
844 doi:10.1002/2016WR019344, 2016.

845 Wu, S. C., Kruizinga, G., and Bertiger, W.: Algorithm theoretical basis document for  
846 GRACE Level-1B data processing V1.2, JPL D-27672, Jet Propul. Lab., Pasadena, Calif,  
847 2006.

848 Xie, Z., Huete, A., Restrepo-Coupea, N., Maa, X., Devadasa, R., Caprarellib, G.: Spatial  
849 partitioning and temporal evolution of Australia's total water storage under extreme  
850 hydroclimatic impacts, *Remote Sens. Environ.*, 183, 43–52,  
851 <http://dx.doi.org/10.1016/j.rse.2016.05.017>, 2016.

852 Zaitchik, B. F., Rodell, M., and Reichle, E. H.: Assimilation of GRACE terrestrial water  
853 storage data into a land surface model: Results for the Mississippi basin, *Amer. Meteor. Soc.*,  
854 *J. Hydrometeor.*, 9, 535–548, 2008.

855

856 **Table 1.** Precipitation data from 7 different products used in this study, the Global Soil  
857 Wetness Project Phase 3 (GSWP3), the Global Land Data Assimilation System (GLDAS),  
858 the Tropical Rainfall Measuring Mission (TRMM), the Modern-Era Retrospective Analysis  
859 for Research and Applications (MERRA), the European Centre for Medium-Range Weather  
860 Forecasts (ECMWF), the Princeton's Global Meteorological Forcing Dataset (Princeton), and  
861 the Precipitation Estimation from Remotely Sensed Information using Artificial Neural  
862 Networks (PERSIANN). The temporal resolution of all products are 3 hours. Most products  
863 are available to present while GSWP3, MERRA, and Princeton terminate earlier.

Product	Availability	Spatial resolution	References
GSWP3	1901/01 – 2010/12	0.5°×0.5°	<a href="http://hydro.iis.u-tokyo.ac.jp/GSWP3">http://hydro.iis.u-tokyo.ac.jp/GSWP3</a>
GLDAS (NOAH025SUBP 3H)	2000/03 – present	0.25°×0.25°	Rodell et al. (2004)
TRMM (3B42)	1998/01 – present	0.25°×0.25°	Huffman et al. (2007)
MERRA (MSTMNXMLD.5.2.0)	1980/01 – 2016/02	0.5°×0.67°	Rienecker et al. (2011)
ECMWF (ERA-Interim)	1979/01 – present	0.75°×0.75°	Dee et al. (2011)
Princeton (V2 0.5°)	1987/01 – 2012/12	0.5°×0.5°	Sheffield et al. (2005)
PERSIANN (3 hr)	2002/03 – present	0.25°×0.25°	Sorooshian et al. (2000)

864

865

866 **Table 2.** Model parameters that are sensitive to SM and GWS estimates. The following  
867 parameters were perturbed using the additive noise with the boundary conditions given in the  
868 last column. The further parameter description can be found in Decker (2015) and Ukkola et  
869 al. (2016).

Parameter	Name	Spatial variability	Perturbed range
$f_{\text{clay}}, f_{\text{sand}}, f_{\text{silt}}$	Fraction of clay, sand, and silt	Yes	0 – 1
$f_{\text{sat}}$	Fraction of grid cell that is saturated	No	810 – 990
$q_{\text{sub}}$	Maximum rate of subsurface drainage assuming a fully saturated soil column	No	0.009 – 0.01
$f_{\text{p}}$	Tunable parameter controlling drainage speed	No	1.9 – 2.2

870

871

872 **Table 3.** NS coefficients between top soil moisture estimates and the satellite soil moisture  
 873 observations from AMSR-E products over 10 different Australian basins. The area-weighted  
 874 average value (AVG) is also shown.

	C-band		X-band	
	CABLE	GC	CABLE	GC
GOC	0.67	0.68	0.58	0.60
IND	0.53	0.54	0.41	0.41
LKE	0.48	0.53	0.36	0.42
MRD	0.77	0.80	0.75	0.78
NEC	0.34	0.39	0.14	0.19
NWP	0.33	0.36	0.38	0.42
SEC	0.68	0.68	0.69	0.71
SWC	0.85	0.85	0.89	0.89
SWP	0.55	0.56	0.46	0.48
TIM	0.44	0.45	0.16	0.16
AVG	0.53	0.56	0.47	0.50

875

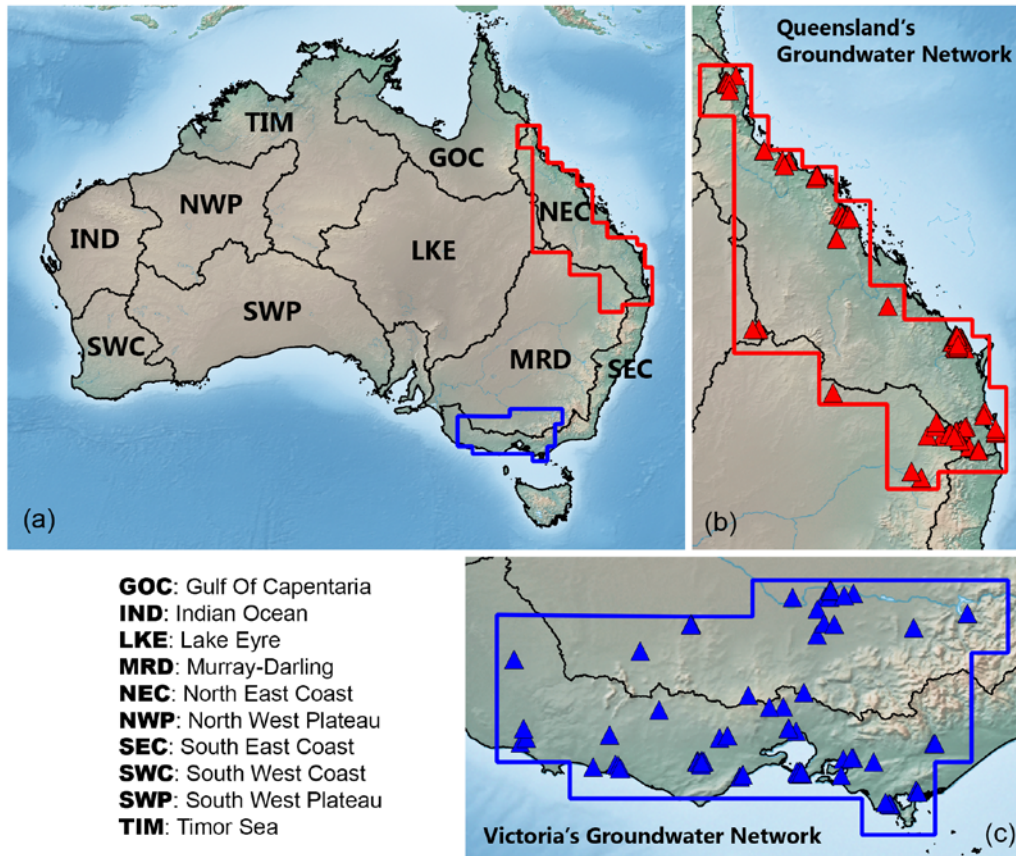
876

877 **Table 4.** NS coefficient and long-term trend of  $\Delta GWS$  estimated from the model-only and  
 878 GC solutions in Queensland and Victoria groundwater network. The long-term trend of the  
 879 in-situ data is also shown.

	Queensland			Victoria		
	In-situ	CABLE	GC	In-situ	CABLE	GC
<b>Original time-series</b>						
NS [-]	-	0.49	0.60	-	0.34	0.63
Trend [cm/year]	$1.60 \pm 0.05$	$0.39 \pm 0.02$	$0.63 \pm 0.05$	$-0.27 \pm 0.05$	$0.10 \pm 0.02$	$-0.18 \pm 0.03$
<b>De-seasonalized time-series</b>						
NS [-]	-	0.50	0.66	-	0.43	0.83
Trend [cm/year]	$1.60 \pm 0.05$	$0.39 \pm 0.02$	$0.57 \pm 0.04$	$-0.25 \pm 0.05$	$0.10 \pm 0.02$	$-0.16 \pm 0.03$

880

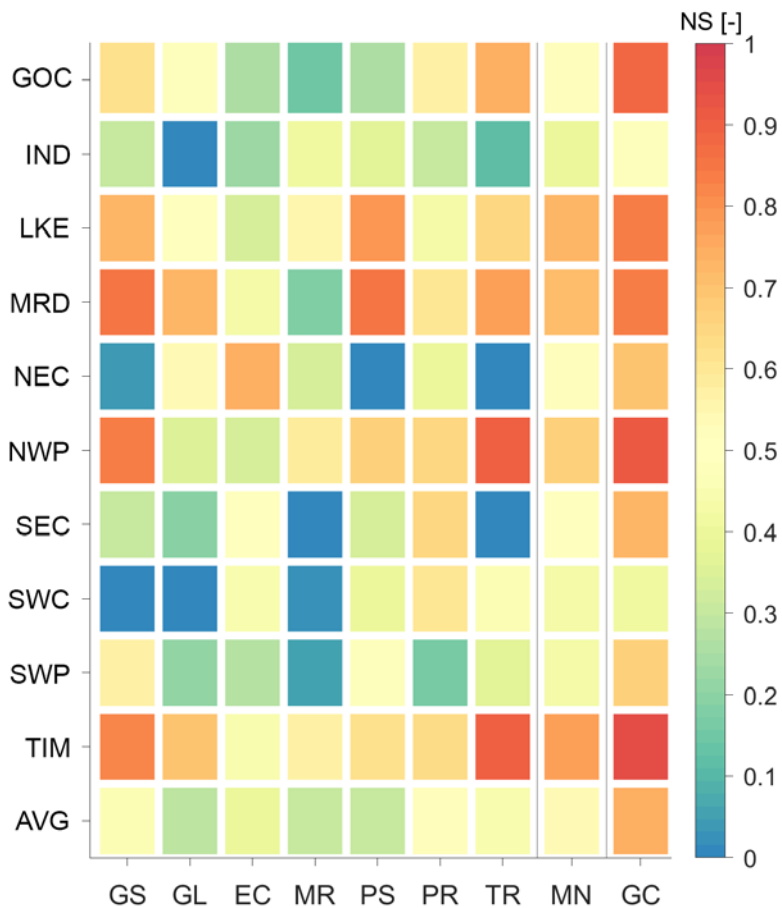




881

882 **Figure 1.** (a) Geographical location of 10 Australian river basins. Red and blue polygons  
 883 indicate the boundaries of groundwater networks in Queensland (b) and Victoria (c),  
 884 respectively. Triangles (in b and c) represent the selected bore locations used in this study.

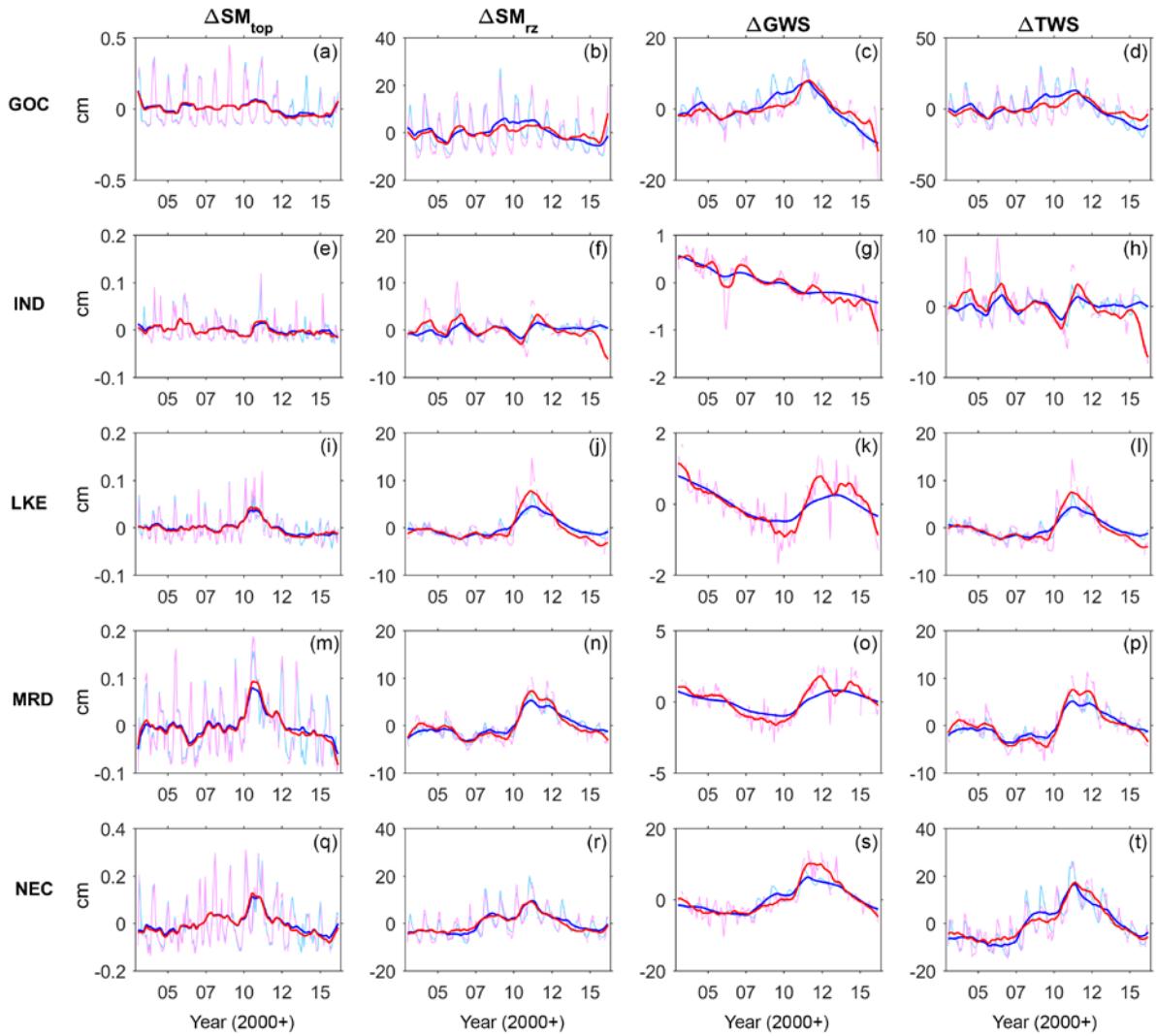
885



886

887 **Figure 2.** NS coefficients between the model and GRACE-mascon  $\Delta TWS$  over 10 Australian  
 888 basins (in ordinate). The NS values were computed based on CABLE  $\Delta TWS$  computed with  
 889 7 different precipitation data (in abscissa), GSWP3 (GS), GLDAS (GL), ECMWF (EC),  
 890 MERRA (MR), PERSIANN (PR), TRMM (TR). The NS value of the mean  $\Delta TWS$  estimates  
 891 (the average of 7 variants) is also shown (MN). The area-weighted average NS value over all  
 892 basins is also shown (AVG). The NS value of  $\Delta TWS$  from the GRACE-combined (GC)  
 893 approach is shown in the last column. The full name of the basins can be found in Fig. 1.

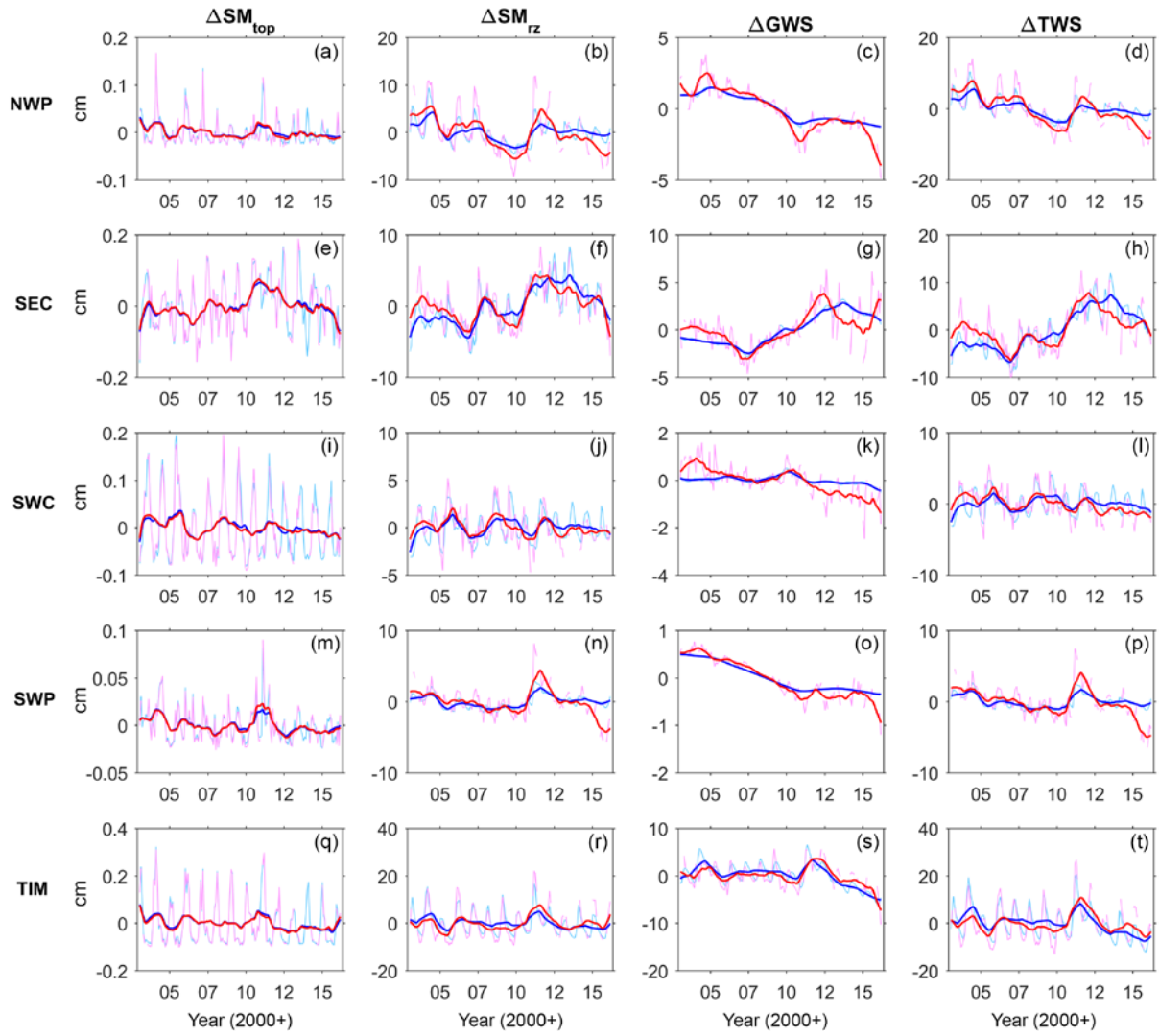
894



895

896 **Figure 3.** The monthly time series of  $\Delta SM_{top}$ ,  $\Delta SM_{rz}$ ,  $\Delta GWS$ , and  $\Delta TWS$  estimated from  
 897 model (blue) and GC (red) solutions over Gulf of Carpentaria (GOC), Indian Ocean (IND),  
 898 Lake Eyre (LKE), Murray-Darling (MRD), and North East Coast (NEC). The de-  
 899 seasonalized time series is also shown.

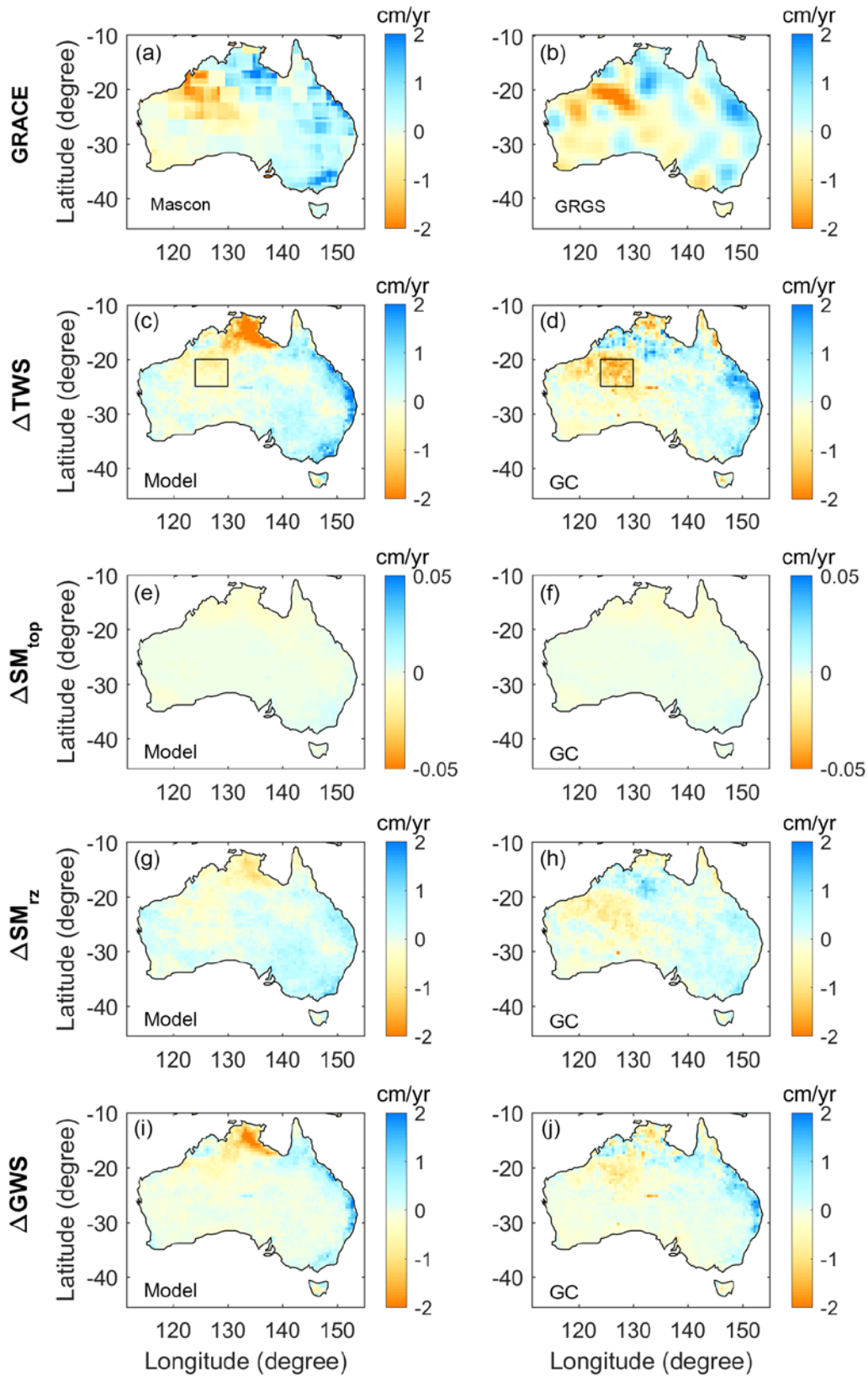
900



901

902 **Figure 4.** Similar to Fig. 3, but estimated over North West Plateau (NWP), South East Coast  
 903 (SEC), South West Coast (SWC), South West Plateau (SWP), and Timor Sea (TIM).

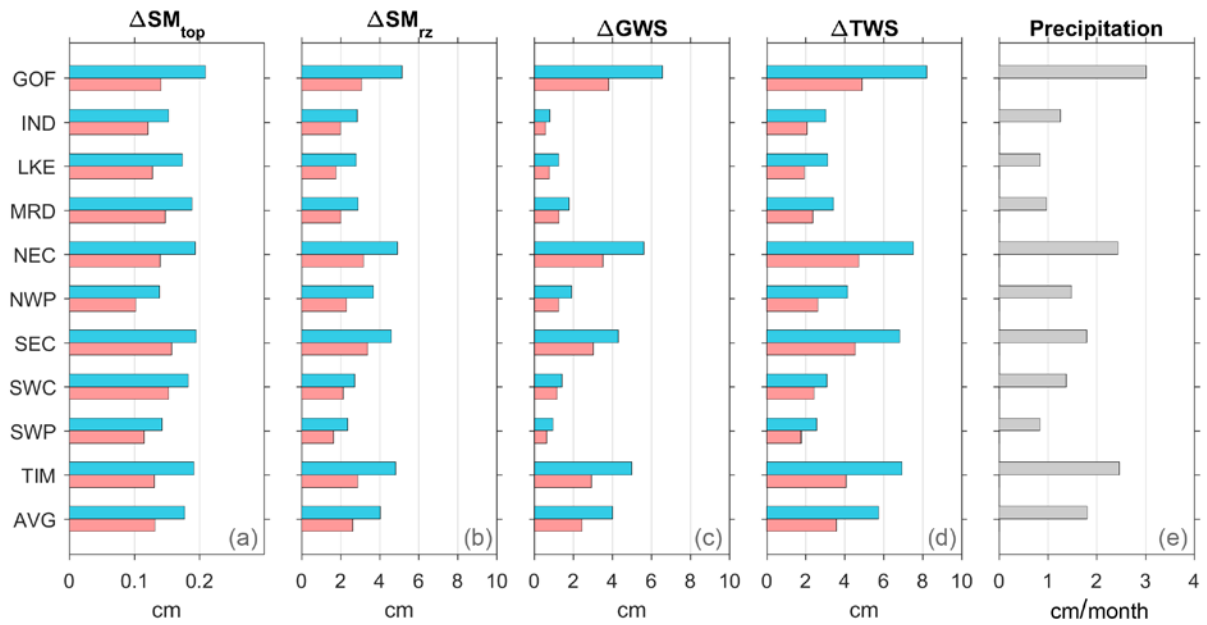
904



905

906 **Figure 5.** Long-term trends of  $\Delta TWS$  (c, d),  $\Delta SM_{top}$  (e, f),  $\Delta SM_{rz}$  (g, h), and  $\Delta GWS$  (i, j)  
 907 estimated from the model-only (left) and the GC solutions (right). Results of GRACE  $\Delta TWS$   
 908 independently from mascon (a) and GRGS solution (b) are also shown. The eastern part of  
 909 North West Plateau basin is shown as a rectangle polygon in (c) and (d).

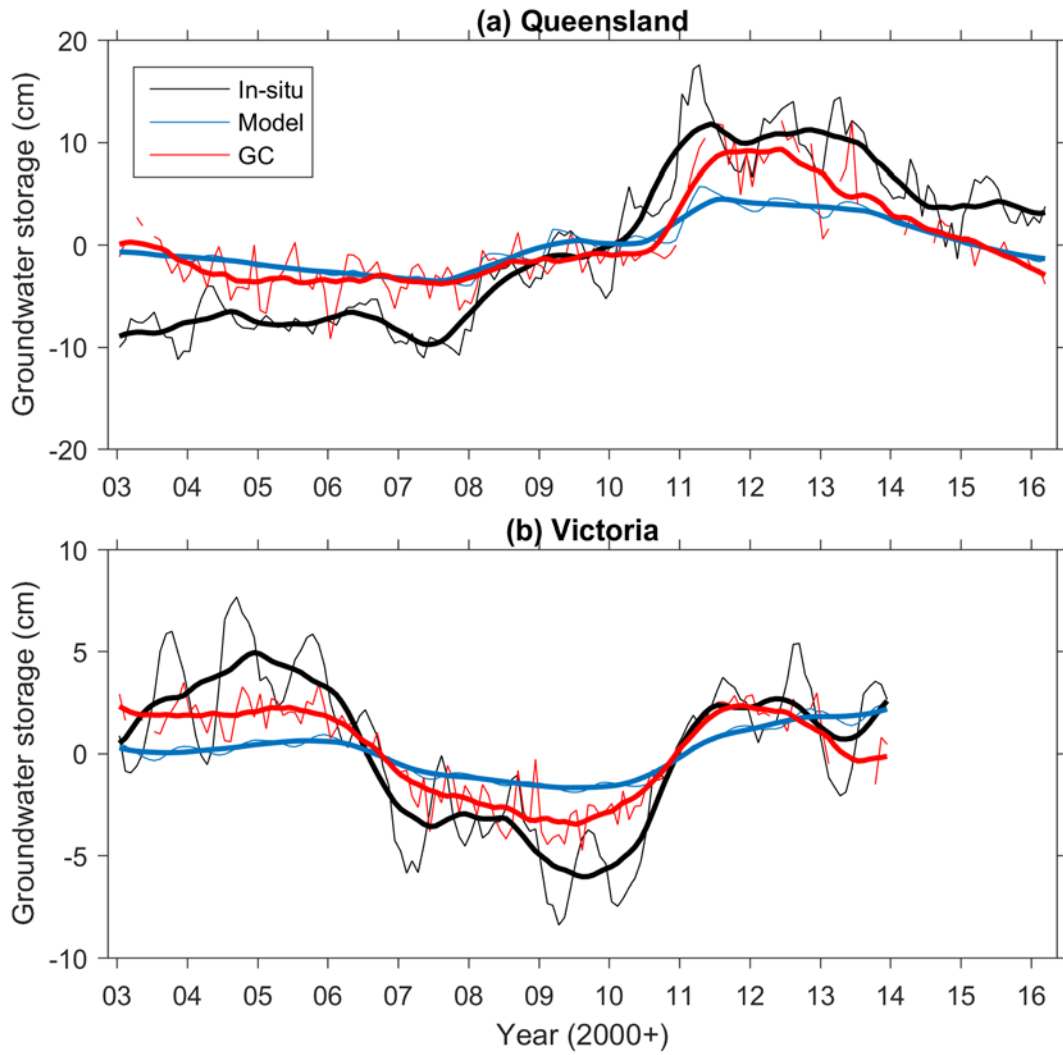
910



911

912 **Figure 6.** Uncertainties of  $\Delta SM_{top}$ ,  $\Delta SM_{rz}$ ,  $\Delta GWS$ , and  $\Delta TWS$  estimated from the model  
 913 (blue) and the GC solutions (red) in 10 different Australian basins. The uncertainty of the  
 914 precipitation is shown in (e). The area-weighted average value (AVG) is also shown.

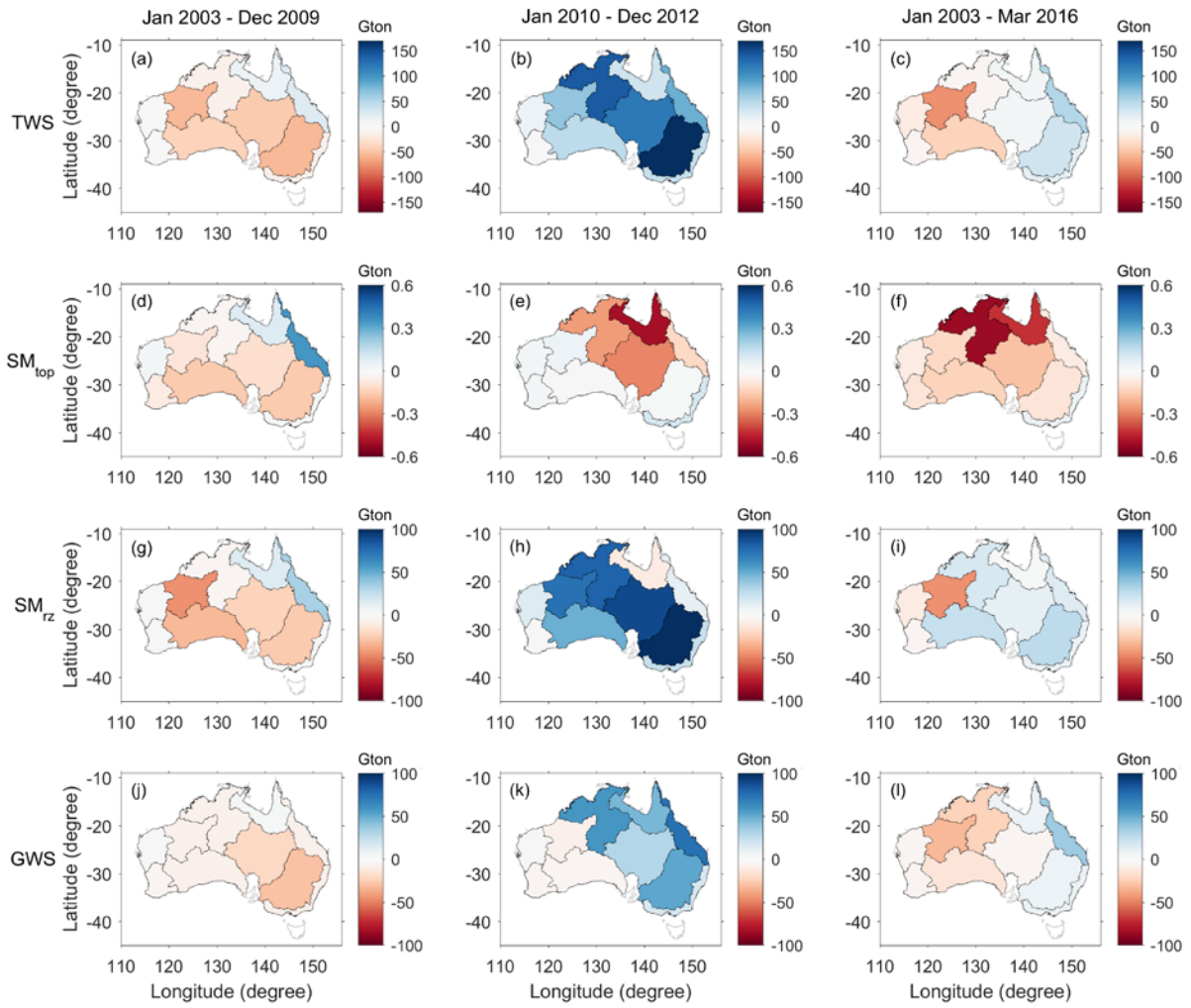
915



916

917 **Figure 7.** The monthly time series of  $\Delta GWS$  estimated from the model, GC solutions, and  
 918 measured from the in situ groundwater network in Queensland (a) and Victoria (b). De-  
 919 seasonalized time series are shown in thick lines.

920

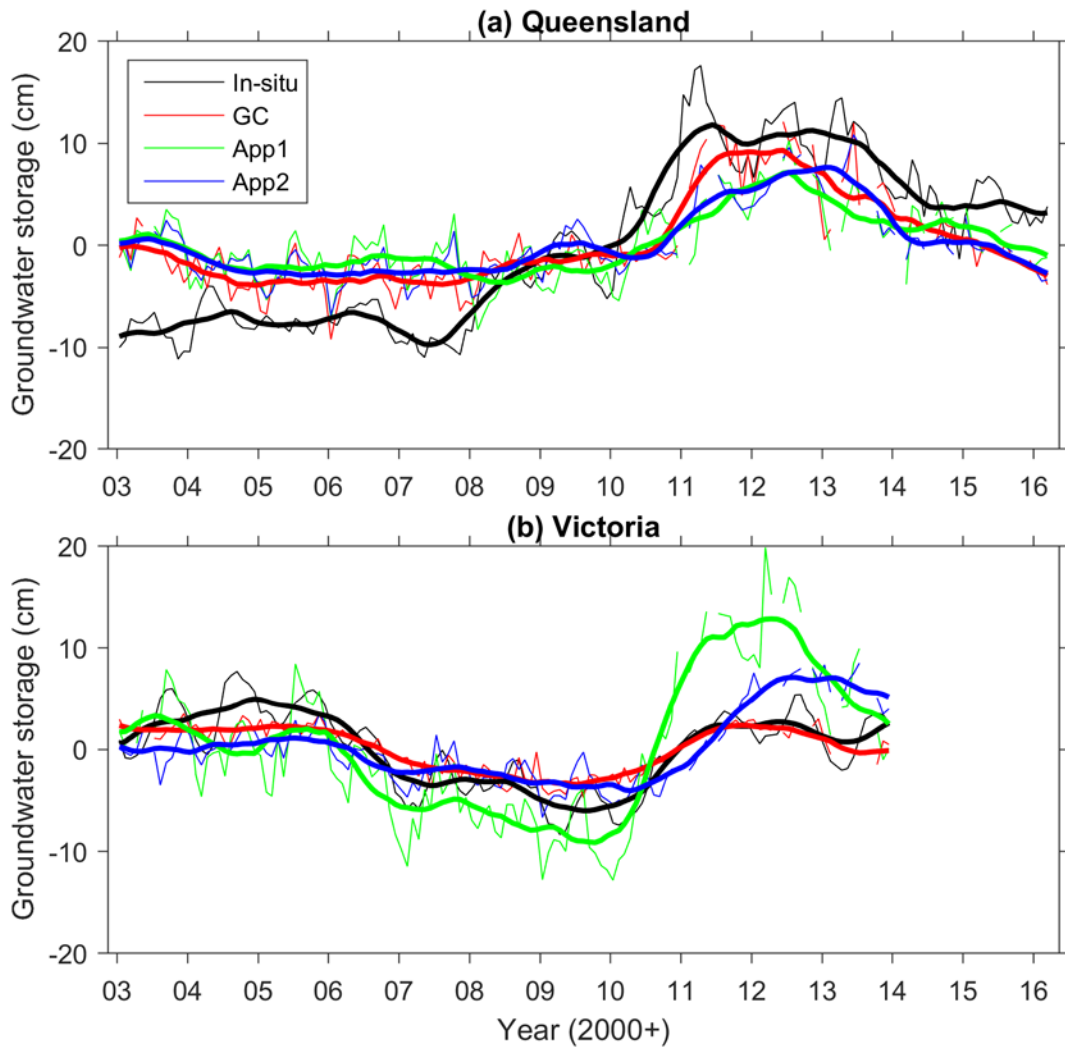


921

922 **Figure 8.** Mass changes (Gton, Giga tonne) of  $\Delta TWS$ ,  $\Delta SM_{top}$ ,  $\Delta SM_{rz}$ , and  $\Delta GWS$  estimated  
 923 from GC solutions over 10 Australian basins in 3 different periods, Big Dry (January 2003 –  
 924 December 2009), Big Wet (January 2010 – December 2012), and entire period (January 2003  
 925 – March 2016).

926





927

928 **Figure 9.**  $\Delta GWS$  estimated from Approach 1 (App1) and Approach 2 (App2) in Queensland  
 929 (a) and Victoria (b). The in-situ groundwater network data and the GC solutions are also  
 930 shown. De-seasonalized time series are shown in thick lines.